ORNL/TM-2016/159

# Linear Array Ultrasonic Test Results from Alkali-Silica Reaction (ASR) Specimens

Dwight Clayton
Lev Khazanovich,
University of Minnesota
Lucio Salles,
University of Minnesota

**April 2016**

OAK RIDGE NATIONAL LABORATORY
MANAGED BY UT-BATTELLE FOR THE US DEPARTMENT OF ENERGY

## DOCUMENT AVAILABILITY

Reports produced after January 1, 1996, are generally available free via US Department of Energy (DOE) SciTech Connect.

**Website** http://www.osti.gov/scitech/

Reports produced before January 1, 1996, may be purchased by members of the public from the following source:

National Technical Information Service
5285 Port Royal Road
Springfield, VA 22161
**Telephone** 703-605-6000 (1-800-553-6847)
**TDD** 703-487-4639
**Fax** 703-605-6900
**E-mail** info@ntis.gov
**Website** http://www.ntis.gov/help/ordermethods.aspx

Reports are available to DOE employees, DOE contractors, Energy Technology Data Exchange representatives, and International Nuclear Information System representatives from the following source:

Office of Scientific and Technical Information
PO Box 62
Oak Ridge, TN 37831
**Telephone** 865-576-8401
**Fax** 865-576-5728
**E-mail** reports@osti.gov
**Website** http://www.osti.gov/contact.html

This report was prepared as an account of work sponsored by an agency of the United States Government. Neither the United States Government nor any agency thereof, nor any of their employees, makes any warranty, express or implied, or assumes any legal liability or responsibility for the accuracy, completeness, or usefulness of any information, apparatus, product, or process disclosed, or represents that its use would not infringe privately owned rights. Reference herein to any specific commercial product, process, or service by trade name, trademark, manufacturer, or otherwise, does not necessarily constitute or imply its endorsement, recommendation, or favoring by the United States Government or any agency thereof. The views and opinions of authors expressed herein do not necessarily state or reflect those of the United States Government or any agency thereof.

**ORNL/TM-2016/159**

Electrical and Electronics Systems Research Division

# LINEAR ARRAY ULTRASONIC TEST RESULTS FROM ALKALI-SILICA REACTION (ASR) SPECIMENS

Dwight Clayton, Oak Ridge National Laboratory
Lev Khazanovich, University of Minnesota
Lucio Salles, University of Minnesota

Date Published: April 2016

Prepared by
OAK RIDGE NATIONAL LABORATORY
Oak Ridge, Tennessee 37831-6283
managed by
UT-BATTELLE, LLC
for the
US DEPARTMENT OF ENERGY
under contract DE-AC05-00OR22725

# CONTENTS

**Page**

LIST OF FIGURES ........ iv
LIST OF TABLES ........ v
ACKNOWLEDGMENTS ........ vi
EXECUTIVE SUMMARY ........ vii
1. INTRODUCTION ........ 1
2. LINEAR ARRAY ULTRASONIC INTRODUCTION ........ 5
3. CONCRETE SPECIMENS FABRICATION AND EXPANSION CONDITIONING ........ 7
4. ULTRASONIC TESTING PROCEDURE ........ 11
5. DATA ANALYSIS ........ 13
6. RESULTS ........ 15
7. PRELIMINARY WAVE PROPOGATION SIMULATION ........ 23
8. CONCLUSIONS ........ 29
9. REFERENCES ........ 31
APPENDIX A. SAFT-PAN RECONTRUCTIONS ........ A-2

# LIST OF FIGURES

Fig. 1. Alkali silica reaction results in a gel that can expand and may cause micro-cracks in concrete. [3] ..... 2
Fig. 2. Specimens (a) Nefertiti, (b) King Tut, (c) Cleopatra and (d) Ramses ..... 7
Fig. 3. Expansion measurement devices ..... 8
Fig. 4. (a) Device positioned at Panoramic 6 on specimen Cleopatra; and (b) Readings layout ..... 11
Fig. 5. SAFT-Pan Reconstruction of specimen Nefertiti, panoramic 3 ..... 16
Fig. 6. SAFT-Pan Reconstruction of specimen Nefertiti, panoramic 5 ..... 16
Fig. 7. SAFT-Pan Reconstructions of specimen King Tut, (a) panoramic 4 and (b) panoramic 6 ..... 17
Fig. 8. SAFT-Pan Reconstruction of specimen Cleopatra, panoramic 5 ..... 17
Fig. 9. SAFT-Pan Reconstruction of specimen Ramses, panoramic 1 ..... 18
Fig. 10. SAFT-Pan Reconstruction of specimen Cleopatra, panoramic 1 ..... 18
Fig. 11. HTI versus shear wave velocity 1 ..... 19
Fig. 12. HTI color map for specimens (a) Nefertiti; (b) Cleopatra; (c) Ramses; and (d) King Tut ..... 20
Fig. 13. Visible cracking in specimens (a) Cleopatra (south) and (b) Ramses (north) ..... 21
Fig. 14. Visible cracking in specimen King Tut. ..... 23
Fig. 15. Simulation scenarios for specimen with three cracks (top), and five cracks (bottom). ..... 24
Fig. 16. Wave propagation in plain concrete specimen (left) and specimen with three 12 mm vertical cracks on the surface (right). ..... 25
Fig. 17. Wave propagation in plain concrete specimen (left) and specimen with five 12-mm vertical cracks on the surface (right). ..... 26
Fig. 18. SAFT reconstructions for undamaged specimen (top), three cracks (center), and five cracks (bottom). ..... 27

## LIST OF TABLES

Table 1. Wave type information ........................................................................................................... 6
Table 2. Mixture proportions for ASR specimens ......................................................................... 8
Table 3. Results Summary ................................................................................................................ 15
Table 4. Slab Expansion and HTI data .......................................................................................... 22
Table 5. Simulation HTI Data.......................................................................................................... 28

# ACKNOWLEDGMENTS

This work is funded by the U.S. Department of Energy's office of Nuclear Energy under the Light Water Reactor Sustainability (LWRS) program. The authors would like to thank Ms. Maria Guimaraes and Mr. Salvador Villalobos at the Electric Power Research Institute (EPRI) for providing access to and the expansion data on the Alkali-Silica Reaction (ASR) specimens.

# EXECUTIVE SUMMARY

The purpose of the U.S. Department of Energy Office of Nuclear Energy's Light Water Reactor Sustainability (LWRS) Program is to develop technologies and other solutions that can improve the reliability, sustain the safety, and extend the operating lifetimes of nuclear power plants (NPPs) beyond 60 years. Since many important safety structures in an NPP are constructed of concrete, inspection techniques must be developed and tested to evaluate the internal condition. In-service containment structures generally do not allow for the destructive measures necessary to validate the accuracy of these inspection techniques. This creates a need for comparative testing of the various nondestructive evaluation (NDE) measurement techniques on concrete specimens with known material properties, voids, internal microstructure flaws, and reinforcement locations.

Alkali-Silica Reaction (ASR) is a reaction that occurs over time in concrete between alkaline cement paste and reactive, non-crystalline silica in aggregates. An expansive gel is formed within the aggregates which results in micro cracks in aggregates and adjacent cement paste. The reaction requires the presence of water and has been predominately detected in ground water impacted portions of below grade structures, with limited impact to exterior surfaces of above grade structures. ASR can potentially affect concrete properties and performance characteristics such as compressive strength, modulus of elasticity, flexural stiffness, shear strength, and tensile strength.

There are currently no NDE methods that have proven effective in identifying ASR before it is visibly detectable. ASR is usually identified either visibly or by petrographic analysis. As a matter of fact, to confirm the presence of ASR at the Seabrook Nuclear Power Station, concrete cores were removed from the "B" Electrical Tunnel and underwent petrographic examination and strength testing. The lack of an effective NDE technique to detect ASR is emphasized by the experiences at Seabrook. This report documents some of the first research steps taken to develop and certify a NDE technique which can give predictive information on the formation of ASR. Since ASR degradation often takes significant amounts of time, developing this ASR detection technique is important to the sustainability and extended operational lifetimes of NPPs.

This report presents results of the ultrasound evaluation of four concrete slabs with varying levels of ASR damage present. This included an investigation of the experimental results, as well as a supplemental simulation considering the effect of ASR damage by elasto-dynamic wave propagation using a finite integration technique method. It was found that the Hilbert Transform Indicator (HTI), developed for quantification of freeze thaw damage in concrete structures, could also be successfully utilized for quantification of ASR damage.

# 1. INTRODUCTION

ORNL/LTR-2013/125 documents several recent concrete issues at nuclear power plants (NPPs) in the United States including delaminations, voids, and Alkali-Silica Reaction (ASR) [1]. As a part of the Seabrook License Renewal process in 2009, basis documents were developed to support the aging management program. Included in these basis documents was a structure monitoring program. As part of the development of these documents, personnel at the Seabrook Station Nuclear Power Plant, which is operated by NEXTera Energy, observed small, shallow cracks on the walls of an electrical routing tunnel; the "B" Electrical Tunnel. This tunnel, housing the wires that connect the reactor control center to electrical equipment throughout the plant, is approximately 100 yards long and is constructed entirely of concrete. This area had been exposed to significant groundwater intrusion for several years. The small, shallow cracks presented a "crazed", "mapped", or "patterned" appearance which when visually observed in concrete structures is typically indicative of a form of concrete degradation known as ASR. Seabrook is the first nuclear NPP in the U.S. nuclear industry to exhibit ASR in concrete structures on site [2].

ASR is a known type of concrete degradation which was first identified in the 1930's and is common in the transportation industry in bridge structures, roads, and airport runways. There are ASTM standards used to specify and test concrete mixes especially in NPPs to help ensure that ASR does not occur in their structures. During the original concrete placements in the late 1970's to mid 1980's, Seabrooks concrete mixes were tested using the accepted test methods at the time, ASTM C289 (Standard Test Method of Potential Alkali-Silica Reactivity of Aggregates [Chemical Method]) and ASTM C295 (Standard Guide for Petrographic Examination of Aggregates for Concrete), and ASR was not predicted by these tests. However, the ASTM Committee on Normal Weight Aggregates, C09.20, has since cautioned that these specific ASTM tests may not accurately predict reactivity of the aggregate when a late or slowly-expanding aggregate is used. Seabrook engineers have confirmed that such an aggregate was used in the Seabrook construction.

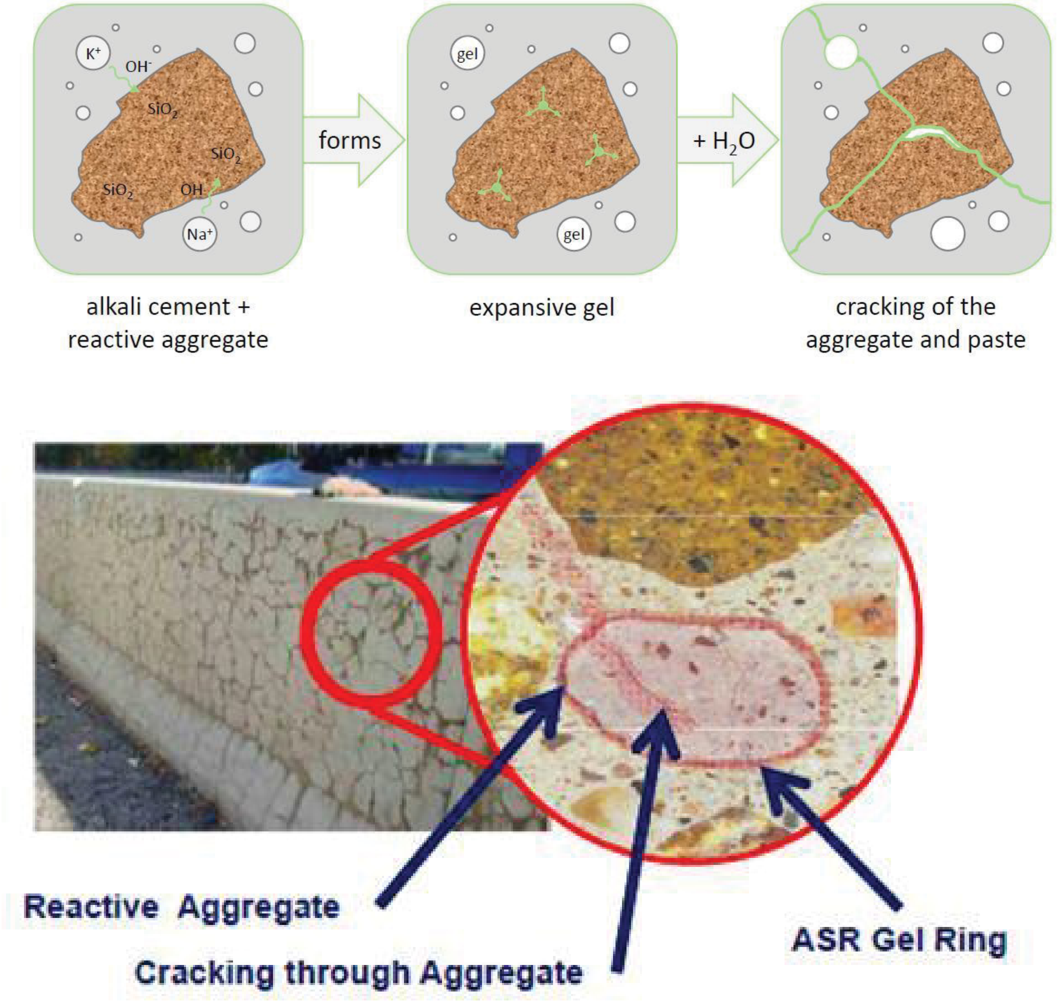

**Fig. 1. Alkali silica reaction results in a gel that can expand and may cause micro-cracks in concrete. [3]**

ASR is a reaction that occurs over time in concrete between alkaline cement paste and reactive, non-crystalline silica in aggregates. An expansive gel is formed within the aggregates which results in micro cracks in aggregates and adjacent cement paste. The reaction requires the presence of water and has been predominately detected in ground water impacted portions of below grade structures, with limited impact to exterior surfaces of above grade structures. ASR can potentially affect concrete properties and performance characteristics such as compressive strength, modulus of elasticity, flexural stiffness, shear strength, and tensile strength. While ASR definitely impacts concrete material properties, the performance of concrete structures exhibiting ASR depends upon if the concrete is unconfined or confined with reinforcing bars. Confinement by reinforcing bars acts to restrain the expansion of ASR affected concrete similar to pre-stressing, thus improving the performance of a structure. Additionally, there is no direct correlation between the mechanical properties of concrete sample cores and the in-situ properties of the concrete when in a structure.

In part because of the Seabrook License Renewal process, the ability to nondestructively evaluate ASR damage in concrete is of interest to many organizations including the Electric Power Research Institute (EPRI) and the United States Deparment of Energy (US DOE. This report summarizes initial findings from ultrasound analysis of four specimens exhibiting various stages of ASR damage as shown in Fig. 1. These four specimens were constructed in June 2015 at EPRI's Charlotte, NC location.

The University of Minnesota tested these slabs using an ultrasonic device called MIRA. The MIRA device has 40 transducers, arranged in columns of 4 transducers, interacting in pairs with spacing ranging from 40 mm to 360 mm. Each transducer acts as a sending and receiving unit, resulting in 45 individual transducer pairs per measurement. A single measurement takes less than two seconds and results in a 2D image. The quantity of data resulting from the analysis allows for the creation of refined images, which is especially useful when considering very heterogeneous materials. Low frequency waves (typically 50 kHz) allow the signal to navigate through the concrete despite the heterogeneous material characteristics. The signals are reflected once an acoustic discontinuity takes place, which is defined as the interface between a medium wherein the impedance of the following medium is different. The acoustic impedance is a material property and is the product of sound velocity and material density.

# 2. LINEAR ARRAY ULTRASONIC INTRODUCTION

A background on elastic wave propagation, which is the basis of the MIRA ultrasonic technique used for initial data collection of the specimen built in this study, allows for a more thorough understanding of the analysis performed. When exposed to a short duration external impact, concrete reacts approximately like an elastic solid medium, where the distortion and subsequent movements in the concrete can be described using three general modes of wave propagation categorized by the coverage and direction of particle motion with respect to propagation direction: p-waves, s-waves, and r-waves.

The compression (also known as longitudinal or primary) waves (p-waves) have particle motion parallel with the direction of wave propagation. The four transverse (also known as shear) waves (s-waves) have particle motion perpendicular to the wave propagation direction. The Rayleigh waves (r-waves) have retrograde elliptical particle motion. The r-waves propagate along the surface, whereas the p- and s-waves propagate throughout the body of the solid in a hyperbolic nature [4]. The reflection of p- and s-waves depends on changes in acoustic impedance from internal characteristics of concrete structures. P- and s-waves are useful in evaluating internal characteristics of concrete structures with only one-sided access because changes in subsurface properties such as flaws, inclusions, or layer boundaries cause reflections back to the surface.

If concrete is approximated as an isotropic and elastic medium, the relationship between elastic parameters (Modulus, Poisson's ratio), density, and wave velocity in concrete has the form shown in Eqs. (1) through (3) [4]:

$$\boldsymbol{C_P} = \sqrt{\frac{\boldsymbol{E(1-\mu)}}{\boldsymbol{(1-\mu)(1-2\mu)\rho}}}\,, \qquad \text{Equation 1}$$

$$\boldsymbol{C_S} = \sqrt{\frac{\boldsymbol{E}}{\boldsymbol{2(1+\mu)\rho}}}\,, \qquad \text{Equation 2}$$

$$\boldsymbol{C_R} = \boldsymbol{C_s}\frac{\boldsymbol{0.87+1.12\mu}}{\boldsymbol{1+\mu}}\,, \qquad \text{Equation 3}$$

where $E$ is Young's modulus of elasticity, μ is Poisson's ratio, ρ is density, $C_P$ is the p-wave velocity, $C_S$ is the s-wave velocity, and $C_R$ r-wave velocity.

Assuming the shear wave response is being evaluated and a typical value for Poisson's ratio in concrete, $\mu = 0.2$, the velocity of the other wave types has the following relationship with respect to s-waves:

$$\boldsymbol{C_S = 0.61C_P = 1.09C_R} \text{ .} \qquad \text{Equation 4}$$

Table 1 gives additional information, including the particle motion, relative wave speeds, and energy content of the various wave types [5].

**Table 1. Wave type information**

| Wave type | Particle motion | Propagation medium | Relative wave speed, $\boldsymbol{\mu = 0.2}$ | Energy content (%) |
|---|---|---|---|---|
| p-wave | Parallel to propagation direction | Solid, liquid, or gas body wave | 0.61 | 7 |
| s-wave | Perpendicular to propagation direction | Solid body wave | 1 | 26 |
| r-wave | Retrograde elliptical | Surface wave | 1.09 | 67 |

A few observations can be made from these relationships with regard to use of elastic waves for evaluation of thick reinforced concrete structures. Since acoustic impedance is positively correlated to the stiffness of the material, elastic waves are extremely proficient at characterizing interfaces such as cracks, voids, or delamination where the change in acoustic impedance from concrete to air is extremely high. However, since Portland cement concrete (PCC) is composed of air voids and aggregates, elastic waves can also experience significant attenuation that limits the penetration depth. For example, since the p-wave has the lowest amount of energy from a point source impact, it may not achieve the necessary penetration depth required to characterize the thick concrete specimen due to the low energy content. However, the ability to propagate in all types of media may provide air-coupled possibilities [6]. S-waves have significantly higher energy content, allowing for greater penetration depth in heterogeneous media such as concrete. However, they require a solid material for propagation, creating a need for ground coupling. Moreover, because they are similar in velocity to r-waves, boundary effect interference may be a problem.

The Elastodynamic Finite Integration Technique (EFIT), developed at the University of Kassel (Germany), is an effective tool for investigating both the penetration depth and the boundary effect challenges in evaluating thick reinforced concrete structures [7]. The EFIT has been used to compare elastic wave propagation in a 2D concrete model assuming 0% and 1% air porosity from a 200 kHz center frequency point source. It was reported that the reflections from simulated inclusions and back wall reflections were less clear with porosity and that the signal-to-noise ratio (SNR) decreased with depth. While evaluation based on lower frequency content may resolve this difficulty, the general trend of increased attenuation and a decreased SNR with depth holds true. Therefore, the same internal defects that can be identified in thin concrete structures may require improved filtering or processing techniques for identification at greater depth due to the decreased SNR. This is especially true for heavily reinforced concrete structures where scattering and reflection of the wavefront occurs at the boundaries between concrete and steel [8]. This decreasing SNR with depth is a significant challenge that needs to be addressed for effective nondestructive characterization of aging concrete material in NPP containment structures.

## 3. CONCRETE SPECIMENS FABRICATION AND EXPANSION CONDITIONING

The concrete slabs used in this study were fabricated by the University of Alabama [9]. Each specimen is 914 mm x 1219 mm (36 in x 48 in) and 203 mm (8 in.) thick (Fig. 2). The concrete mix was designed with highly reactive aggregates for three specimens (King Tut, Cleopatra and Ramses), while the control specimen (Nefertiti) was designed with unreactive materials. The mixture for the three reactive specimens contained a non-reactive coarse aggregate (NCA) from Calera, AL, a highly-reactive fine aggregate (RFA) from El Paso, TX, and Type I/II PCC from Leeds, AL. Sodium hydroxide was used in these slabs to raise their equivalent alkali content to 1.25% by mass of cement. For Nefertiti a NCA from Calera, AL (#67 size), a non-reactive fine aggregate (NFA) from Calera, AL, and Type I/II PCC from Leeds, AL were utilized. The water /cement ratio for all specimens was fixed at 0.50. Table 2 provides the mixture proportions for the reactive and non-reactive specimens. Additional chemical and physical properties of the cement and aggregates can be found in Klenke and Giannini (2015).

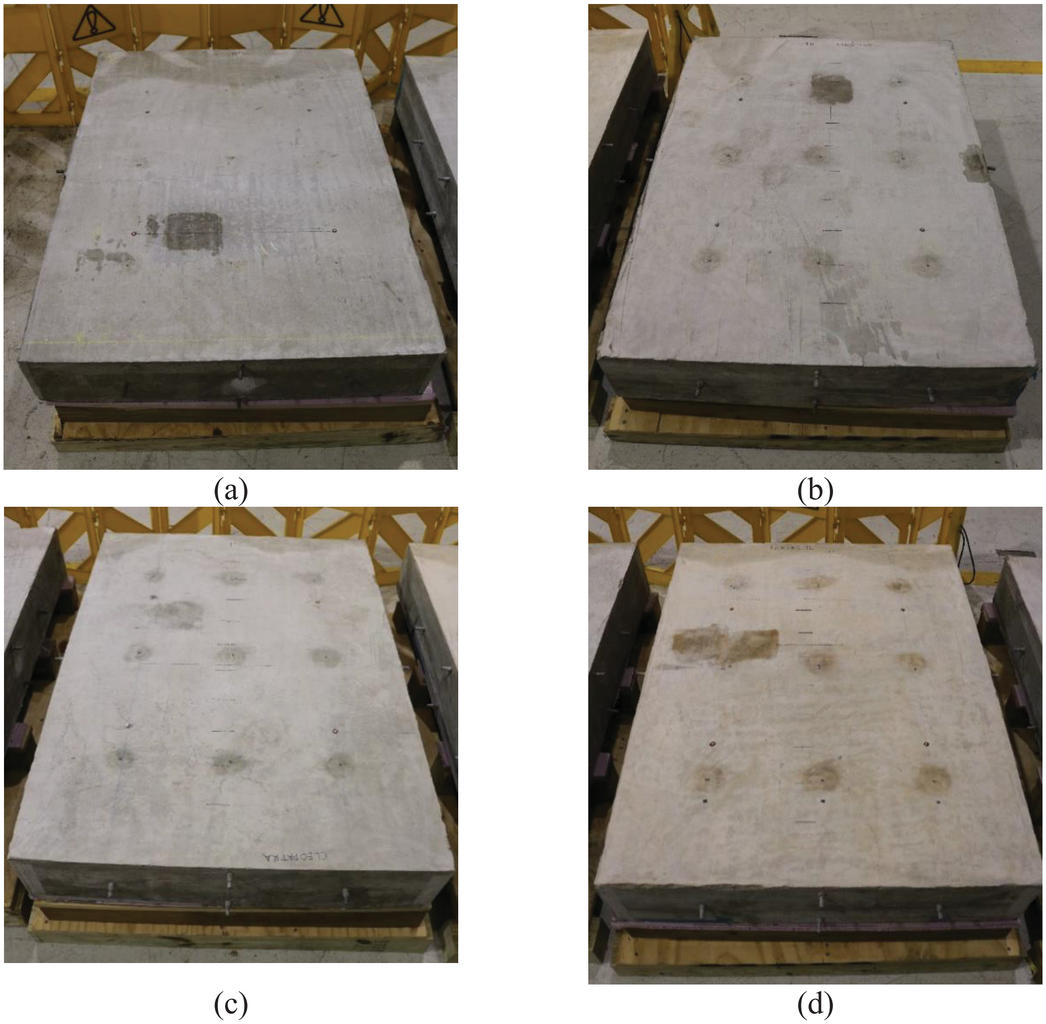

(a) (b) (c) (d)

Fig. 2. Specimens (a) Nefertiti, (b) King Tut, (c) Cleopatra and (d) Ramses

**Table 2. Mixture proportions for ASR specimens**

| Material | ASR Control | ASR Reactive |
|---|---|---|
|  | kg/m$^3$ (lb/yd$^3$) |  |
| Cement | 420 (708) | 420 (708) |
| Water | 210 (354) | 210 (354) |
| NCA* | 1095 (1845) | 1095 (1845) |
| RFA* | – | 608 (1025) |
| NFA* | 639 (1077) | – |
| NaOH | – | 7.0 (11.8) |

*Oven dry

In order to facilitate expansion measurements, hex bolts with conical targets for Demountable Mechanical Strain Gague DEMEC gauge measurements were threaded into the formwork and embedded into the concrete. Four hex bolts were placed in each side of the specimens. Bolt spacing was fixed at 500 mm (19.7 in.) and at 150 mm (5.9 in.) for horizontal and vertical expansion measurements, respectively. After casting, four additional DEMEC target discs were attached to the top of each specimen in a 500 mm (19.7 inch) square. Fig. 3 shows the expansions measurement devices described above.

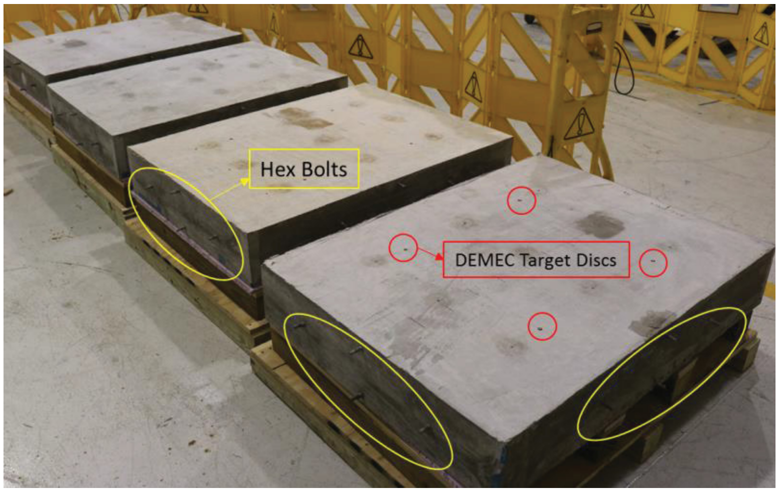

**Fig. 3. Expansion measurement devices**

The curing process took seven days after casting. During the first four days, the specimens were covered with wet burlap. For the remaining days the specimens were placed in an environmental chamber set at 23 °C and covered in wet burlap and plastic. Following the curing process, the reactive specimens were placed in environmental chambers with a set temperature of 38 °C and 98% relative humidity. The environmental chamber conditions were altered to 23 °C and 50% relative humidity during expansion testing days. The control specimen was left in the concrete lab set to 23 °C and 50 % relative humidity. When the reactive slabs reached their target expansions, the specimens were moved to an isolated environmental chamber set to 10 °C and 30% relative humidity to slow the reaction and associated expansion. Reactive specimens Ramses and Cleopatra were stored at the lower temperature and relative humidity environment for four days while King Tut was stored in this environment for only three days. The control specimen (Nefertiti) remained in the 23 °C and 50 % relative humidity environment. Expansion measurements for the specimens were taken weekly using Mayes Instruments DEMEC gauges. As the slabs approached their target expansions, measurements were increased to twice per week. Expansion was characterized by average top surface expansions only.

## 4. ULTRASONIC TESTING PROCEDURE

Fig. 5 shows the device used for this study along with a layout of scan locations. The scans were taken in sets of 11 positions in 50 mm step sizes moving north to south. The device was placed 50 mm off the north edge of the slab. These overlapping scans were used to create extended Synthetic Aperture Focusing Technique (SAFT) subsurface panoramic reconstructions (SAFT-Pan) along the specimen length. It can also be observed that this set of 11 scans was taken in six panoramic locations in 125 mm step sizes moving east to west, corresponding to the width of the device. This allowed for the creation of six SAFT-Pan reconstructions per set of 66 measurements on each slab. The measurement procedure was adopted based on a similar analysis on specimens with freeze and thaw damage [10].

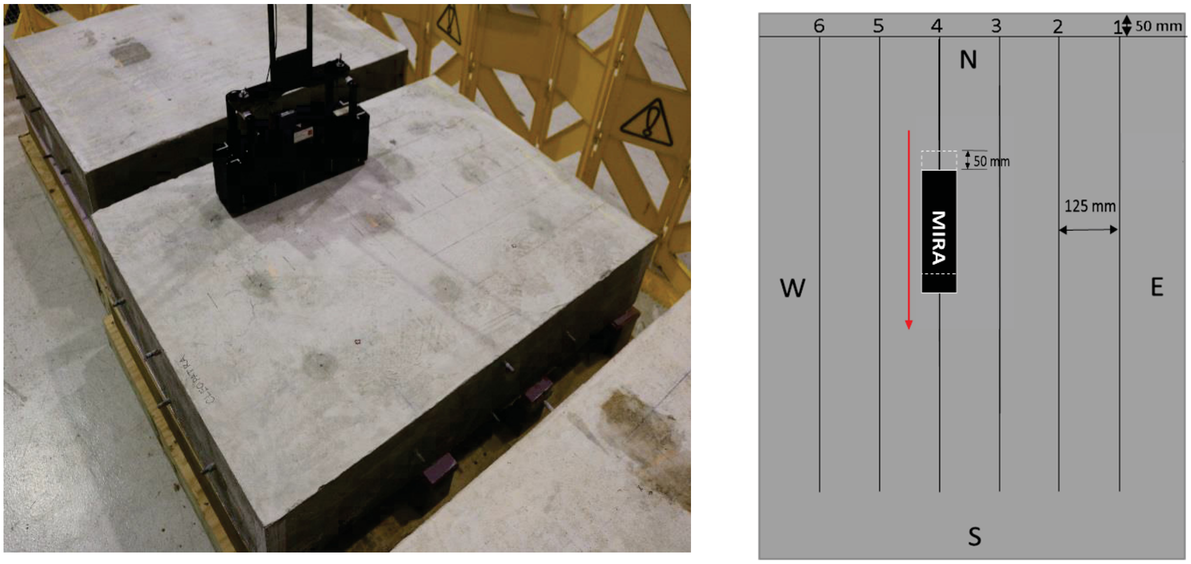

(a) (b)

**Fig. 4. (a) Device positioned at Panoramic 6 on specimen Cleopatra; and (b) Readings layout**

# 5. DATA ANALYSIS

## 5.1. PANORAMIC RECONSTRUCTIONS

The experimental investigation yielded six rows of 11 overlapping MIRA scans per slab. The measurements from each row of scans were used to create panoramic reconstructions. This was achieved via the creation of SAFT reconstructions from reflection portions of the 45 signals from each individual scan. While box software included with the device can yield SAFT reconstructions, a signature technique was utilized in this research in order to achieve greater freedom in the handling of variables. Reconstructions provide focused images showing the presence of damage or inclusions, or in undamaged cases, the presence of only the backwall. Combining these individual SAFT reconstructions into one comprehensive panoramic reconstruction allows for analysis of the entire cross section and reduce signal to noise effects caused by the heterogeneous nature of concrete [11].

The following equation allows for the creation of the SAFT reconstructions:

$$\hat{\boldsymbol{o}}(x,z) = \int_{x'_{min}}^{x'_{max}} \alpha(x',x,z)\, s\left(x', \frac{2}{c}\sqrt{z^2+(x-x')^2}\right) dx' \qquad \text{Equation 5}$$

where α(x',x,z) is the apodization factor [12], *x'*$x'_{min}$ and $x'_{max}$ are the interval in which the signals are measured, *c* is the sound velocity, *x* and *z* are the horizontal and vertical positions in the region of interest (ROI), *x'* is the transducer location, and *s* is the received impulse. The apodization factor accounts for the multiple incident angles incorporated by the array.

However, these SAFT reconstructions have their limitations. The edges of each scan reconstruction spans only 400 mm, making comprehensive cross section analysis difficult. To incorporate greater confidence and redundancy by capitalizing on the overlapping nature of the 11 measurements, panoramic reconstructions can improve the results via the compiling individual SAFT reconstructions. The following equation is used to combine the individual reconstructions to create the panoramic reconstructions which have a larger ROI:

$$\widehat{\boldsymbol{O}}_{PAN}^{m}(x,z) = \begin{cases} \widehat{\boldsymbol{O}}_{PAN}^{m-1}(x,z), & if\ x < D \\ \max\left(\widehat{\boldsymbol{O}}_{PAN}^{m-1}(x,z), \widehat{\boldsymbol{O}}_{I}^{m}\ (\mathrm{x,z})\right), & \mathrm{if\ D} < \mathrm{x} < x_{PAN}^{m-1} \\ \widehat{\boldsymbol{O}}_{I}^{m}\ (\mathrm{x,z}), & if\ x > x_{I}^{m} \end{cases} \qquad \text{Equation 6}$$

where each SAFT scan, $\widehat{\boldsymbol{O}}_{I}^{m}$, where *m* is the index of the current SAFT scan and *I* denotes that it is an individual scan, is combined to form the new region of interest, $ROI_{PAN}^{m}$. This region has a vertical dimension of z and a horizontal dimension of $x_{PAN}^{m}$, in this case 900 mm, and D is the distance from the global origin [12], [13], [14]. For each panoramic reconstruction in this study, 11 individual SAFT scans were merged in this manner [15].

## 5.3. QUANTITATIVE INDICATOR

In order to determine the level of damage present in the slabs in a quantitative and non-subjective manner, the Hilbert Transform Indicator (HTI) was utilized for slab characterization. This indicator is based upon the signal characteristics which ~~clean~~ undamaged concrete exhibits, allowing for variations from this sound condition to be seen numerically. This value is shown below in mathematical form in Equation 1:

$$HTI = \int_0^{500} \frac{HT(t)}{\max(HT(t))} \, dt \qquad \text{Equation 7}$$

where HT(t) is the Hilbert transform envelope. As such, a higher HTI value would be indicative of damaged concrete, while a low value represents sound concrete. This is due to the increased oscillation in the signal present for damaged concrete conditions, which increases the instantaneous amplitude envelope. In general, values below 90 are regarded as an indicator of sound concrete while values above 100 indicate the initial development of damage. Extensive damage results in HTI values in the range of 120-160 [10].

# 6. RESULTS

Table 3 gives an averaged summary of results. The specimen's name and location 1 to 6 (east to west) are presented. Results show the average parameter value for the 11 individual scan locations. Also displayed is the average values for s-wave velocity at the concrete surface. Moreover, the reflection at the specimen's bottom (thickness) was used for analysis of the damage condition. Plain concrete in sound condition is expected to have a strong relative reflectivity at the thickness interface or "back wall" as compared to its shallower features when evaluating the SAFT-Pan reconstructions. Based on this visual assumption, the last column of Table 3 brings the location quality categorization of "sound", "partial damage" and "damaged", as follows:

- 1: Sound – Reconstructions showing a strong and continuous relative reflectivity at the "back wall" as compared to its shallower features.
- 2: Partial Damage – Reconstructions exhibiting a strong back wall reflection at selected locations along with features indicating presence of damage such as a discontinuity in the backwall reflection or high noise-to-signal ratio at shallower depths.
- 3: Damaged – Reconstructions showing no presence of a back wall reflection either due to prohibitive noise at shallower depths or attenuation of the signal prior to arrival at the concrete depth.

**Table 3. Results Summary**

| SLAB | PANORAMIC | HTI | VEL. (m/ms) | CONCRETE CONDITION |
|---|---|---|---|---|
| Nefertiti | 1 | 74.95 | 2.349 | Sound |
| | 2 | 68.26 | 2.407 | Sound |
| | 3 | 69.49 | 2.417 | Sound |
| | 4 | 66.95 | 2.412 | Sound |
| | 5 | 72.67 | 2.297 | Sound |
| | 6 | 71.42 | 2.451 | Sound |
| King Tut | 1 | 90.98 | 2.128 | Partial Damage |
| | 2 | 83.91 | 2.122 | Sound |
| | 3 | 79.67 | 2.131 | Sound |
| | 4 | 81.08 | 2.133 | Sound |
| | 5 | 85.96 | 2.133 | Sound |
| | 6 | 88.82 | 2.146 | Partial Damage |
| Cleopatra | 1 | 104.31 | 2.118 | Partial Damage |
| | 2 | 106.87 | 2.142 | Partial Damage |
| | 3 | 110.11 | 2.144 | Partial Damage |
| | 4 | 101.71 | 2.157 | Partial Damage |
| | 5 | 107.23 | 2.162 | Partial Damage |
| | 6 | 105.39 | 2.124 | Partial Damage |
| Ramses | 1 | 108.03 | 2.096 | Partial Damage |
| | 2 | 97.01 | 2.148 | Partial Damage |
| | 3 | 105.97 | 2.130 | Partial Damage |
| | 4 | 108.31 | 2.102 | Partial Damage |
| | 5 | 105.31 | 2.129 | Partial Damage |
| | 6 | 109.50 | 2.100 | Partial Damage |

Since the initial categorization is very general, reconstructions that are slightly different can fit in the same category. A few examples with commentary will be shown in this section. An exhaustive set of SAFT-Pan reconstructions can be found in Appendix A. It is also worth noting that as no reconstruction achieved the third categorization level (damaged), there are only examples of the first two categories. Fig. 5 and Fig. 6 shown below, are both taken from specimen Nefertiti and are representative of the sound concrete condition seen for all panoramics taken from this slab. Fig. 5 is a reconstruction taken in the middle of specimen Nefertiti (3rd SAFT-Pan). While this scan shows a sound concrete condition with a continuous back wall reflection spanning the width of the reconstruction, slightly more attenuation of the back wall reflection was observed around the 300 mm marking. This may indicate the presence of a distress in development or poor concrete consolidation being reflected above the backwall. The same happens to panoramic 5 in specimen Nefertiti (Fig. 6). Fig. 6 is still representative of sound concrete, but a weaker reflection after the middle of the reconstruction (400 mm marking) is present. This indicates a more sound concrete in the north region of the specimen than in the south.

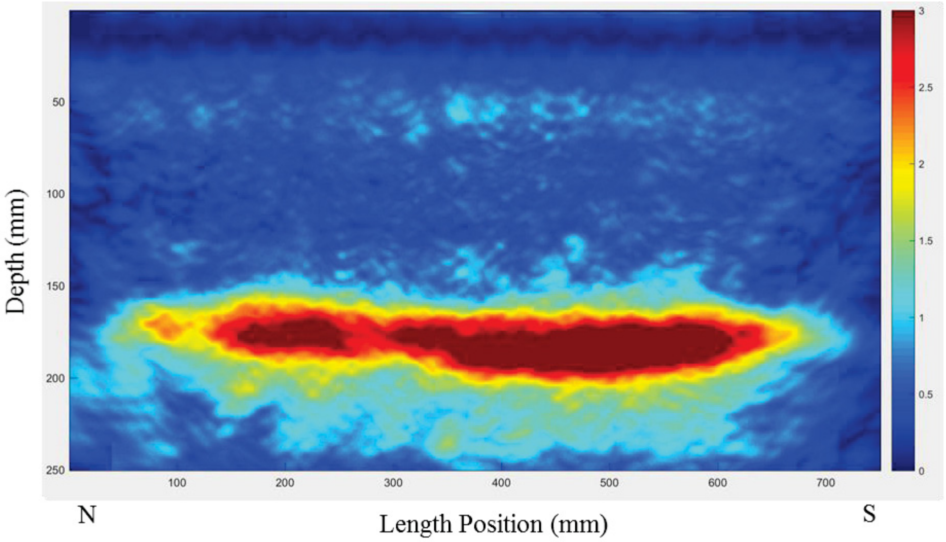

**Fig. 5. SAFT-Pan Reconstruction of specimen Nefertiti, panoramic 3**

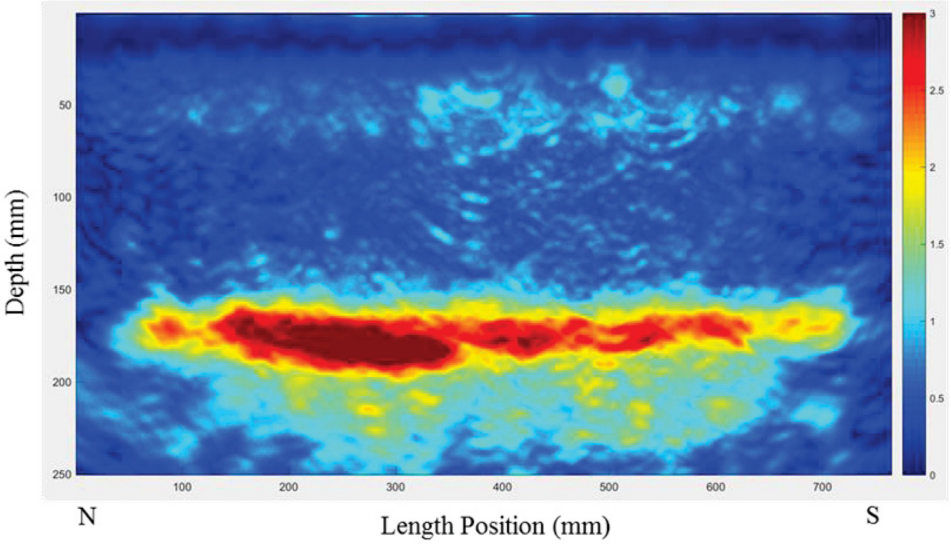

**Fig. 6. SAFT-Pan Reconstruction of specimen Nefertiti, panoramic 5**

Specimen King Tut presents both characterizations “sound” and “partial damage”. Reconstructions of these conditions are shown in Fig. 7. Fig. 7(a) displays the middle of specimen King Tut (4th SAFT-Pan) showing a clear, sound concrete condition with a continuous and uniform back wall reflection throughout the width of the reconstruction. On the other hand, Fig. 7(b) (6th SAFT-Pan) presents more attenuation indicating the existence of partial damage.

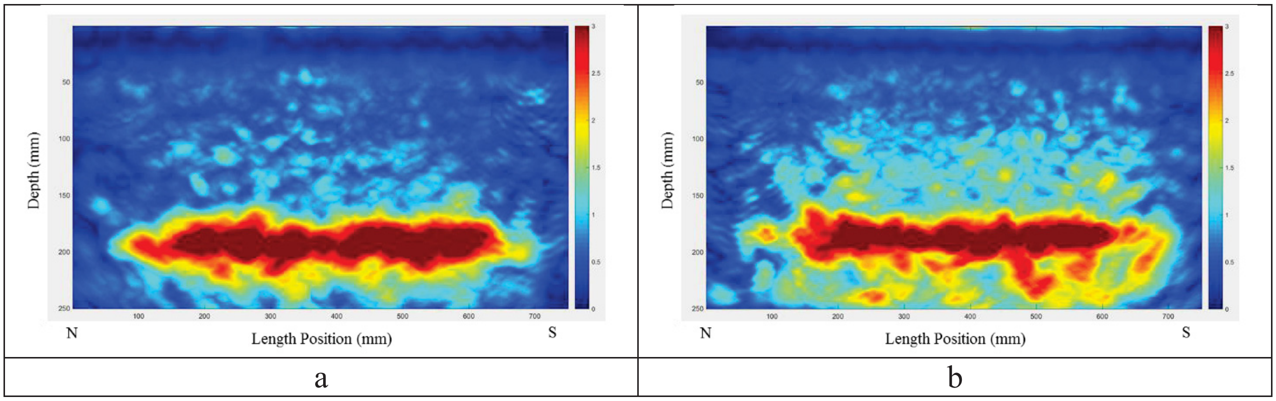

a

b

**Fig. 7. SAFT-Pan Reconstructions of specimen King Tut, (a) panoramic 4 and (b) panoramic 6**

Fig. 8 through Fig. 10 show reconstructions which serve as examples that indicate a slightly damaged concrete condition (partial damage). Fig. 8 was taken on the west side of specimen Cleopatra (5th SAFT-Pan). It shows a mostly sound concrete condition with a continuous and uniform back wall reflection in the middle of the reconstruction. However, the breaks in backwall continuity at the edges of the reconstructions, in conjunction with more attenuate reflections near the backwall, indicates the damage presence. Fig. 9 shows a reconstruction for specimen Ramses (1st SAFT-Pan) with more strong reflections and a clear break in the back wall at the end of the reconstruction (South area). In both cases, attenuation from damage could have shadowed the backwall in some parts of the reconstruction.

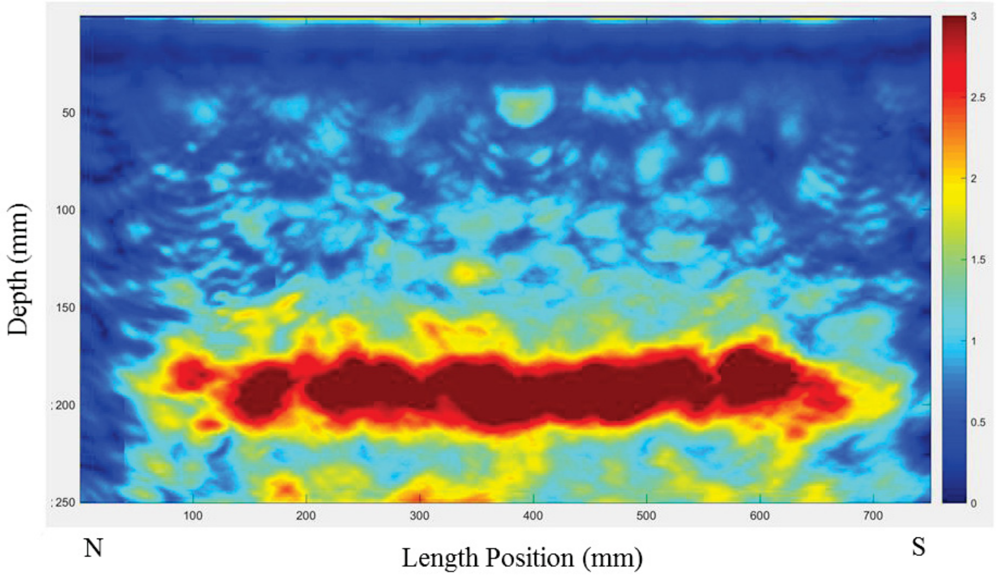

**Fig. 8. SAFT-Pan Reconstruction of specimen Cleopatra, panoramic 5**

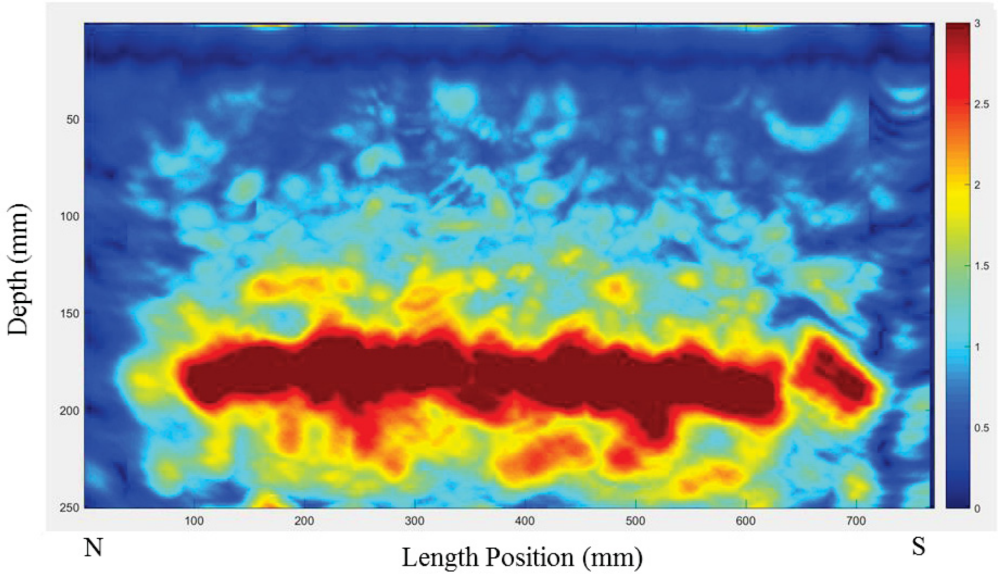

**Fig. 9. SAFT-Pan Reconstruction of specimen Ramses, panoramic 1**

Fig. 10 was taken in the east side of specimen Cleopatra (1st SAFT-Pan). The reconstruction shows a possible distress in the middle of the specimen (red reflection above the backwall). This reflection has a shadowing effect on the back wall right before and after the reflection position. Also, the North part of the specimen presents a weaker back wall than the South part, indicating a more damaged condition. It is again worth noting that these panoramic reconstructions show partial damage conditions, or the early onset of degradation, with no panoramic reconstructions showing severe damage.

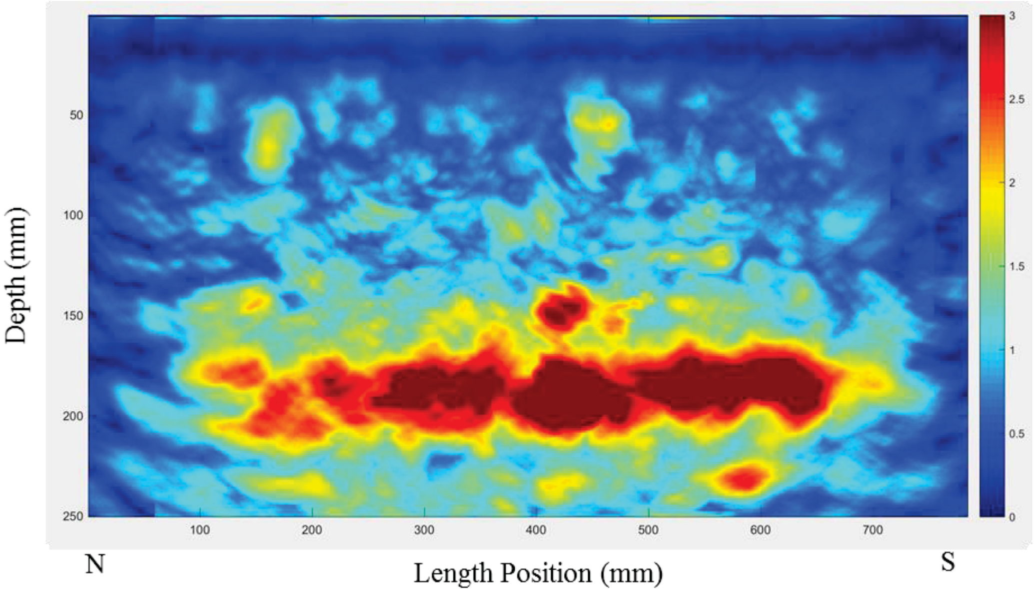

**Fig. 10. SAFT-Pan Reconstruction of specimen Cleopatra, panoramic 1**

Fig. 11shows the relation between the HTI and the s-wave velocity. As can be seen, the control specimen (Nefertiti) presents HTI values consistently below 80, while the s-wave velocity varies greatly. The most damaged specimens (Cleopatra and Ramses) show most scans with HTI values above 100 and low velocity. Specimen King Tut shows what can be interpreted as the first stages of damage. Only three values presented HTI values above 100, with the remaining values averaging around 85. The specimen has reactive aggregate but still presents concrete in mostly sound conditions, as shown by the majority of low HTI values throughout the slab.

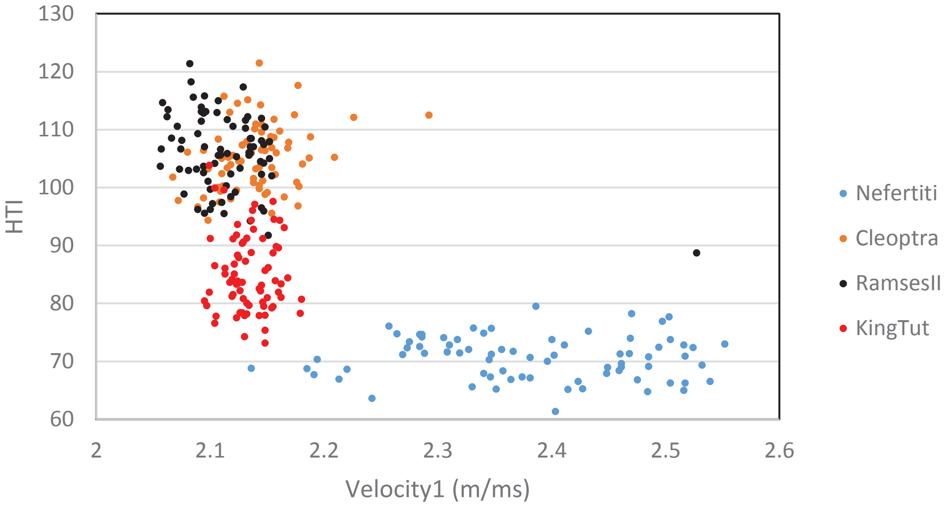

**Fig. 11. HTI versus shear wave velocity 1**

Fig. 12 presents the HTI color map for the four specimens based on results from all scans. According to the HTI value, stronger red tones indicate a more damaged area. The maps show a slab in good condition for the control specimen, Nefertiti, while specimens Cleopatra and Ramses present higher levels of damage. It should be noted that extreme damage conditions were not present in any of the slabs, as would be indicated by a deep red color. Specimen King Tut, as shown by the reconstructions, has both damaged and sound concrete conditions indicating the early stages of damage progression.

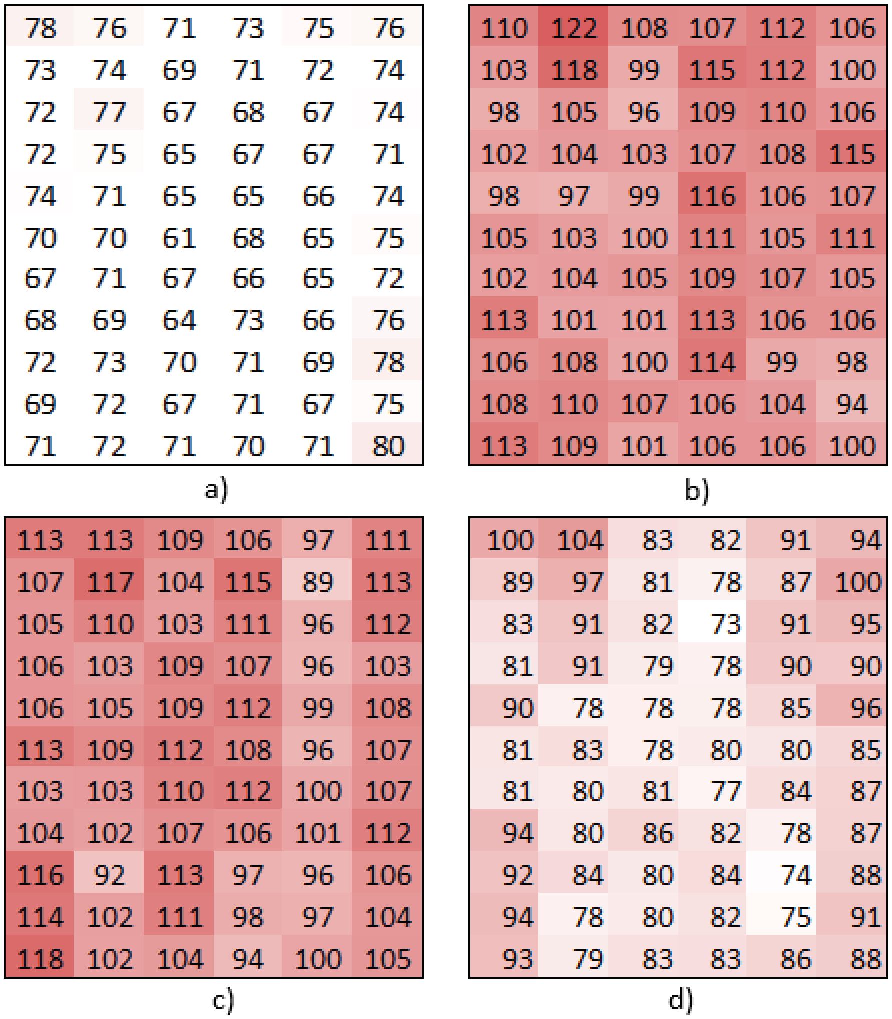

|  |  |  |  |  |  |
|---|---|---|---|---|---|
| 78 | 76 | 71 | 73 | 75 | 76 |
| 73 | 74 | 69 | 71 | 72 | 74 |
| 72 | 77 | 67 | 68 | 67 | 74 |
| 72 | 75 | 65 | 67 | 67 | 71 |
| 74 | 71 | 65 | 65 | 66 | 74 |
| 70 | 70 | 61 | 68 | 65 | 75 |
| 67 | 71 | 67 | 66 | 65 | 72 |
| 68 | 69 | 64 | 73 | 66 | 76 |
| 72 | 73 | 70 | 71 | 69 | 78 |
| 69 | 72 | 67 | 71 | 67 | 75 |
| 71 | 72 | 71 | 70 | 71 | 80 |

a)

|  |  |  |  |  |  |
|---|---|---|---|---|---|
| 110 | 122 | 108 | 107 | 112 | 106 |
| 103 | 118 | 99 | 115 | 112 | 100 |
| 98 | 105 | 96 | 109 | 110 | 106 |
| 102 | 104 | 103 | 107 | 108 | 115 |
| 98 | 97 | 99 | 116 | 106 | 107 |
| 105 | 103 | 100 | 111 | 105 | 111 |
| 102 | 104 | 105 | 109 | 107 | 105 |
| 113 | 101 | 101 | 113 | 106 | 106 |
| 106 | 108 | 100 | 114 | 99 | 98 |
| 108 | 110 | 107 | 106 | 104 | 94 |
| 113 | 109 | 101 | 106 | 106 | 100 |

b)

|  |  |  |  |  |  |
|---|---|---|---|---|---|
| 113 | 113 | 109 | 106 | 97 | 111 |
| 107 | 117 | 104 | 115 | 89 | 113 |
| 105 | 110 | 103 | 111 | 96 | 112 |
| 106 | 103 | 109 | 107 | 96 | 103 |
| 106 | 105 | 109 | 112 | 99 | 108 |
| 113 | 109 | 112 | 108 | 96 | 107 |
| 103 | 103 | 110 | 112 | 100 | 107 |
| 104 | 102 | 107 | 106 | 101 | 112 |
| 116 | 92 | 113 | 97 | 96 | 106 |
| 114 | 102 | 111 | 98 | 97 | 104 |
| 118 | 102 | 104 | 94 | 100 | 105 |

c)

|  |  |  |  |  |  |
|---|---|---|---|---|---|
| 100 | 104 | 83 | 82 | 91 | 94 |
| 89 | 97 | 81 | 78 | 87 | 100 |
| 83 | 91 | 82 | 73 | 91 | 95 |
| 81 | 91 | 79 | 78 | 90 | 90 |
| 90 | 78 | 78 | 78 | 85 | 96 |
| 81 | 83 | 78 | 80 | 80 | 85 |
| 81 | 80 | 81 | 77 | 84 | 87 |
| 94 | 80 | 86 | 82 | 78 | 87 |
| 92 | 84 | 80 | 84 | 74 | 88 |
| 94 | 78 | 80 | 82 | 75 | 91 |
| 93 | 79 | 83 | 83 | 86 | 88 |

d)

**Fig. 12. HTI color map for specimens (a) Nefertiti; (b) Cleopatra; (c) Ramses; and (d) King Tut**

Examination of surface cracking in all specimens confirms the damage presence on specimens Cleopatra and Ramses, as shown in Fig. 13 with cracks highlighted for greater ease of identification. The blue rectangle on Fig. 13(a) shows an enlarged section of the specimen in order for cracks to be more easily visible. Fig. 13 shows minimal visible cracking on the King Tut specimen. Specimen Nefertiti did not have any visible surface cracks.

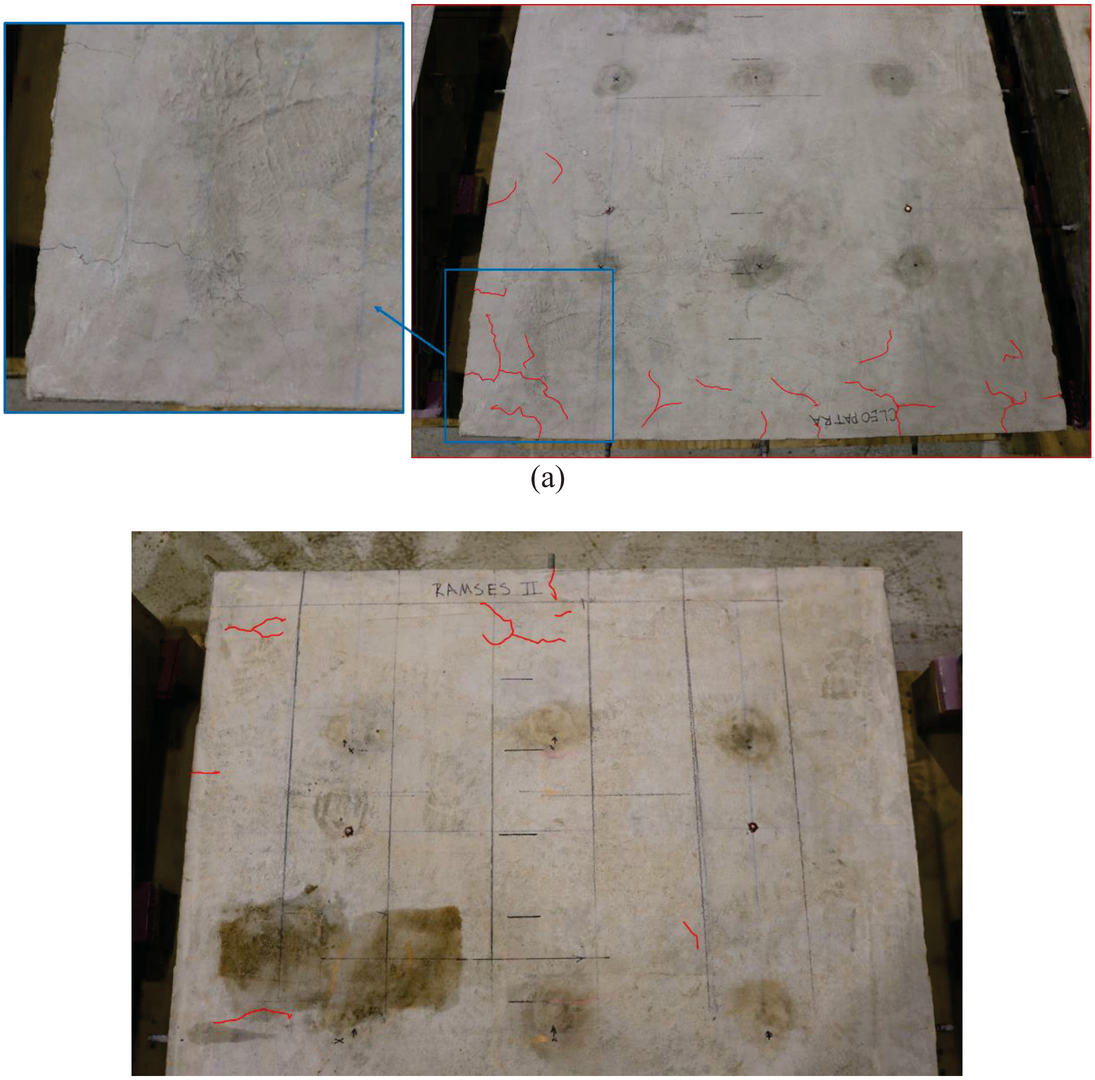

(a)

(b)

**Fig. 13. Visible cracking in specimens (a) Cleopatra (south) and (b) Ramses (north)**

The expansion values for each slab are shown in Table 4 in two different times: firstly at 45 days right before the specimens were shipped to EPRI (Klenke and Giannini, 2015) and at 215 days (Janurary 6th), 20 days before the MIRA testing. Table 4 also brings the average HTI values for each slab. Again, these average HTI values are the result of the averaging of all 66 scan values, with each individual scan containing 45 individual HTI values as a result of the transducer pairs.

As can be seen, there is good agreement between the expansion and HTI values. An additional comparative analysis was performed on the panoramic reconstructions obtained from the slabs. This analysis utilized an adaptation of Pearson's correlation coefficient in order to detect changes in reconstruction matrices which would be indicative of degradation [16]. This analysis compares a reconstruction with a representative sound reconstruction in order to detect the presence of damage. As such, high values are indicative of high correlation, and thus sound concrete. Low values are indicative of the presence of degradation. While the results of this analysis further confirmed the damage levels of the slabs, the small variations in the results were not conclusive enough to draw conclusions from.

**Table 4. Slab Expansion and HTI data**

| Slab | Expansion (45 days) | Expansion (215 days) | Average HTI | HTI (Std) | Pearson's $R^2$ |
|---|---|---|---|---|---|
| Nefertiti | -0.012% | -0.0278% | 70.6 | 2.70 | 0.957 |
| Ramses | 0.087% | 0.179% | 105.7 | 4.13 | 0.952 |
| Cleopatra | 0.046% | 0.141% | 105.9 | 2.61 | 0.927 |
| King Tut | 0.057% | 0.091% | 85.1 | 4.00 | 0.926 |

For further information and all applicable SAFT-Pan reconstructions, see Appendix A.

## 7. PRELIMINARY WAVE PROPOGATION SIMULATION

While the results from the reconstruction and numerical indicator analysis were promising, and showed the ability of this technology to diagnose the condition of the concrete slabs, more knowledge is desired as to why these differences occur. This supplemental information can be gathered through the utilization of a recently developed program which aims to simulate the wave propagation and signal results which are seen in the MIRA output. This simulation program is based on the EFIT. In EFIT, partial differential equations are replaced by integral equations. The integrals are then approximated on finite volumes or cells. Assuming linear interpolation of the integrand, mean value is approximated by the value of the integrand in the center of the cells or its edges. EFIT serves as an efficient numerical approach to study wave propagation in homogeneous and strongly heterogeneous, isotropic, and anisotropic linear and nonlinear elastic media [18], which make it an ideal method to study ultrasonic waves in concrete. This method also allows for flexibility in handling various boundary conditions. For these reasons, EFIT was chosen for this simulation program.

Several cross section cases were run through the simulation in order to determine the effect of damage on the simulated MIRA results. The three cases which were considered are:

No damage present

Three 12-mm cracks at surface

Five 12-mm cracks at surface

Schematics of the two damaged cases are shown below in Fig. 14

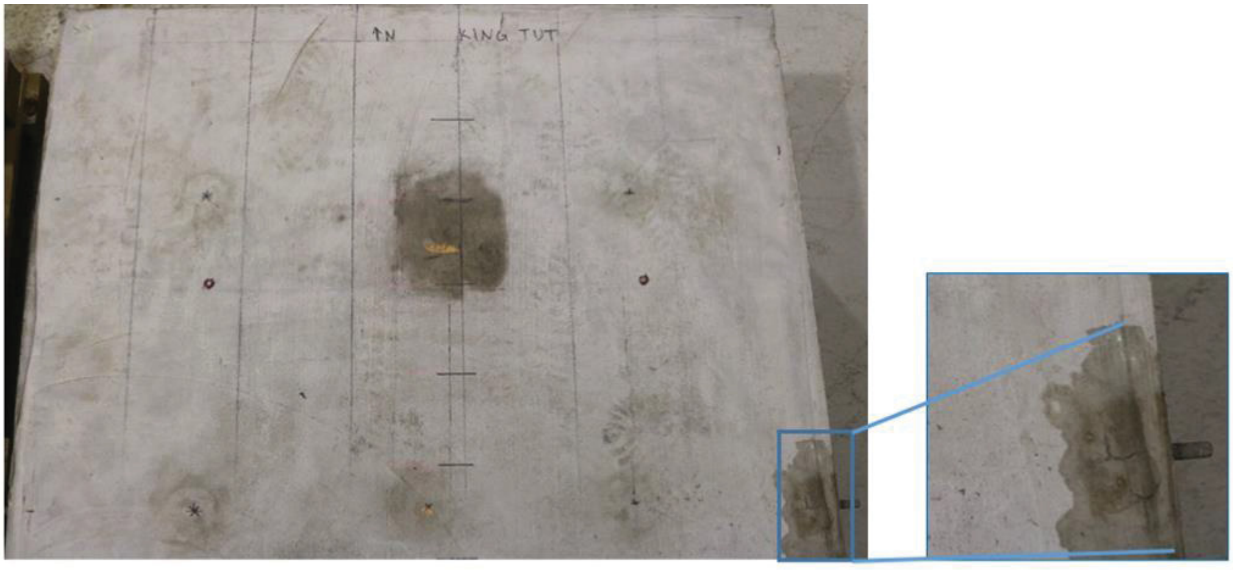

Fig. 14. Visible cracking in specimen King Tut.

To illustrate the effect of the presence of cracks on wave propagation, Fig. 15 shows incremental wave propagation paths for the undamaged concrete (left) and for the slab with three cracks (right). It is clear that the presence of these cracks alters the wave path, as would be expected.

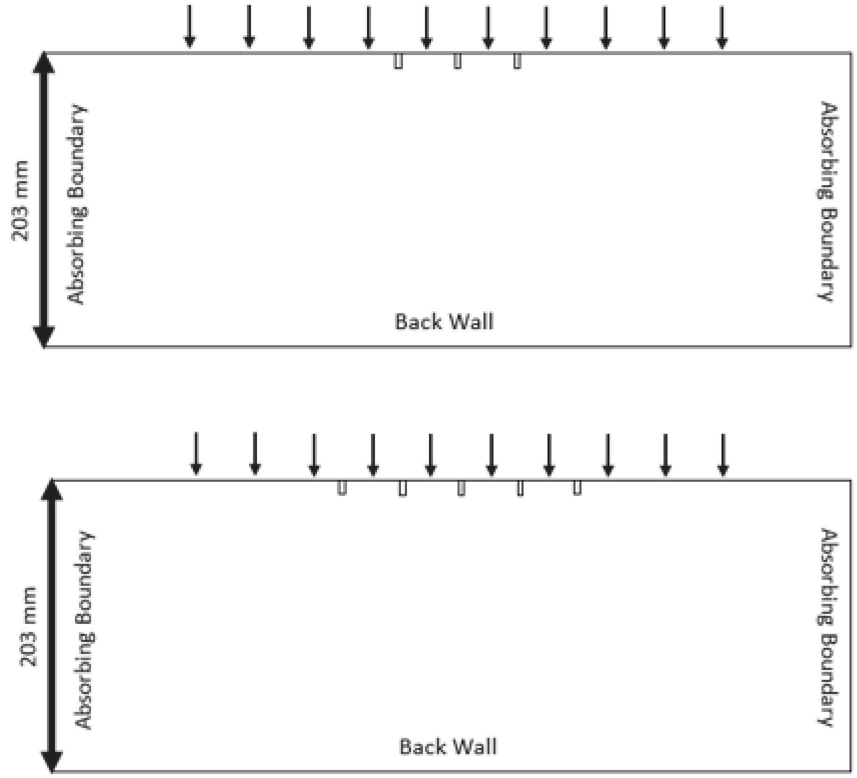

**Fig. 15. Simulation scenarios for specimen with three cracks (top), and five cracks (bottom).**

These same images were created for comparison of the plain specimen and the specimen with five vertical cracks, and is shown in Fig. 16.

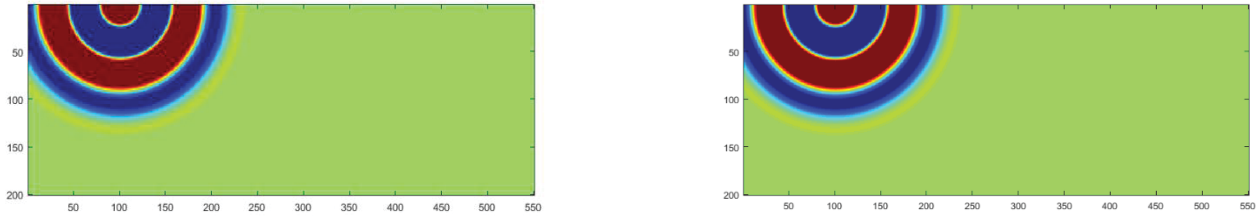

t = 0.00006 s

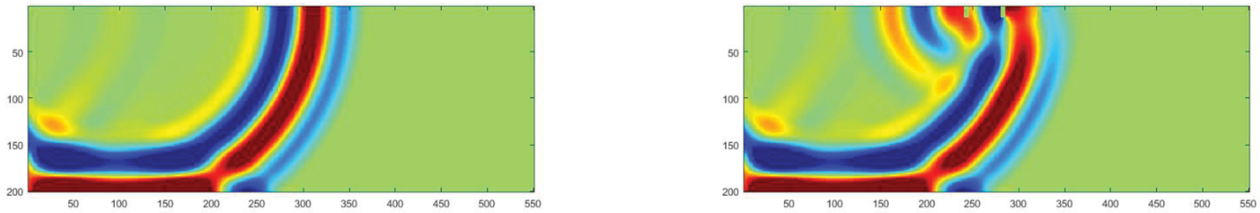

t = 0.00012 s

t = 0.00018 s

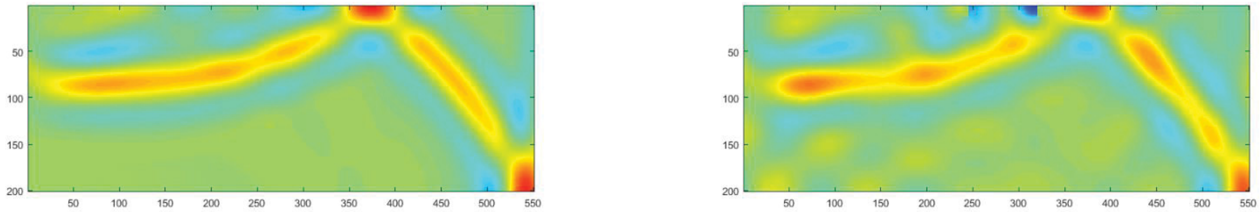

t = 0.00024 s

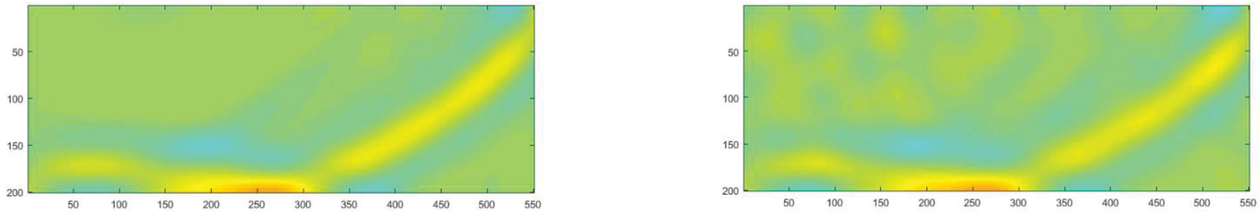

t = 0.00030 s

**Fig. 16. Wave propagation in plain concrete specimen (left) and specimen with three 12 mm vertical cracks on the surface (right).**

The output of the simulation program is in the same format as the raw MIRA output, so the creation of SAFT B-scan reconstructions is also possible. SAFT reconstructions were created for the three cases, and are shown in Fig. 17. These reconstructions show that the specimen with three cracks shows minimal signs of increased reflectivity, while the specimen with five cracks has a reconstruction which makes the damage presence clear with higher reflectivity present at shallower depths than the back wall.

t = 0.00006 s

t = 0.00012 s

t = 0.00018 s

t = 0.00024 s

t = 0.00030 s

**Fig. 17. Wave propagation in plain concrete specimen (left) and specimen with five 12-mm vertical cracks on the surface (right).**

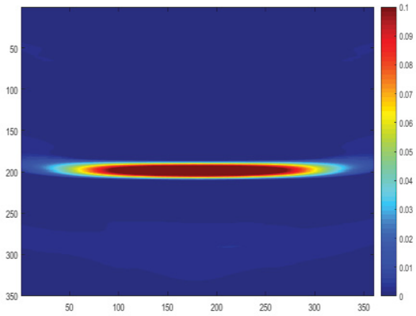

Plain/Undamaged Concrete

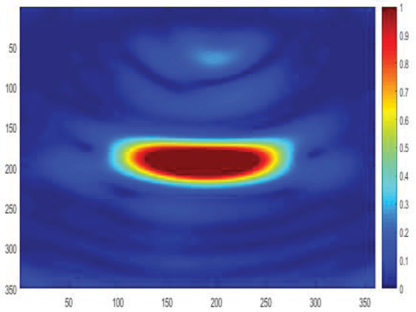

Three 12-mm long vertical cracks on the surface

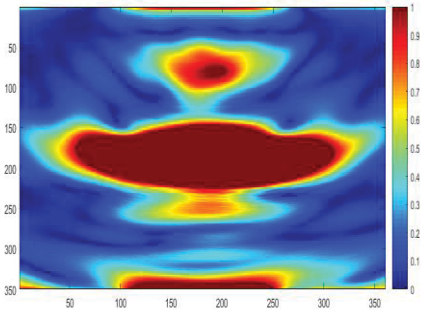

Five 12 mm-long vertical cracks on the surface

**Fig. 18. SAFT reconstructions for undamaged specimen (top), three cracks (center), and five cracks (bottom).**

The results from the HTI analysis for the three cases are shown below in Table 5. For the undamaged specimen, the simulated HTI value corresponds to the magnitudes seen in the control slab (Nefertiti) during the experimental investigation. The specimen with three cracks exhibits HTI values closer to those seen in the partially damaged slabs (King Tut). At the same time, the panoramic reconstructions did not exhibit significant increased reflectivity. Finally, the specimen with five cracks exhibited HTI values which aligned well with those seen in the most damaged slabs (Cleopatra and Ramses). However, the simulated panoramic reconstruction for this case exhibited significant damage which is not necessarily observed from field measurement-based panoramic reconstructions. Therefore, it can be concluded that although the proposed simulation shows great promise to provide insight on the effect of damage in concrete on measured signals, more work is required to achieve good agreement between experimental and simulated results.

**Table 5. Simulation HTI Data**

| Simulation Case | Average HTI |
|---|---|
| Undamaged | 60.3 |
| Three cracks | 90.8 |
| Five cracks | 106.2 |

# 8. CONCLUSIONS

This report presented results of the ultrasound evaluation of four concrete slabs with varying levels of ASR damage present. This included an investigation of the experimental results, as well as a supplemental simulation considering the effect of ASR damage by elasto-dynamic wave propagation using a finite integration technique method. It was found that the Hilbert Transform Indicator (HTI), developed for quantification of freeze thaw damage in concrete structures, could also be successfully utilized for quantification of ASR damage. The elasto-dynamic simulation confirmed that the presence of cracks at the surface increases the HTI values. It was also seen that systems with a greater number of cracks exhibited higher values.

At the same time, this index provides a composite assessment of the level of damage, while not allowing the quantification of the depth or distribution of ASR damage to be known. The simulation of the various damage scenarios using finite integration techniques offers a great potential to obtain a more in-depth understanding of the effect of damage on wave propagation. The preliminary results are promising; however, further improvements to the simulation are necessary in order to ensure that the program is accurately modeling the physical properties of concrete. Additionally, more verification with experimental data is needed. Once the simulation has been adequately improved, an inverse analysis scheme can be developed for improved quantification of the distribution of ASR damage in concrete structures.

# 9. REFERENCES

[1] D. Clayton and C. Smith, "Summary of Recent Concrete Issues at Nuclear Power Plants," Oak Ridge National Laboratory, 2013.

[2] Nuclear Regulatory Commission, "Special NRC Oversight at Seabrook Nuclear Power Plant: Concrete Degradation," 2 November 2012. [Online]. Available: http://www.nrc.gov/info-finder/reactor/seabrook/concrete-degradation.html-summary. [Accessed 1 April 2016].

[3] Nuclear Regulatory Commission, "Seabrook Station Safety in Light of Alkali-Silica Reaction Occurring in Plant Structures," 2012.

[4] F. Schubert and B. Kohler, "Ten Lectures on Impact-Echo," *Journal of Nondestructive Evaluation,* vol. 27, pp. 1-3, 5-21, 2008.

[5] A. Taffe, K. Borchardt and H. Wiggenhauser, "Specimen for the Improvement of NDT Methods - Design and Construction of a Large Concrete Slab for NDT Methods at BAM," in *International Symposium Non-Destructive Testing in Civil Engineering*, 2003.

[6] J. Zhu and J. Popovics, "Imaging Concrete Structures Using Air-Coupled Impact-Echo," *Journal of Engineering Mechanics,* vol. 133, no. C, pp. 628 - 640, 2007.

[7] P. e. a. Fellinger, "Numerical Modeling of Elastic Wave Propagation and Scattering with EFIT - Elastodynamic Finite Integration Technique," *Wave Motion,* vol. 21, no. 1, pp. 47-66, 1995.

[8] F. Schubert and R. Marklein, "Numerical Computation of Ultrasonic Wave Propogation in Concrete Using the Elastodynamic Finite Integration Technique (EFIT)," in *Ultrasonic Symposium*, 2002.

[9] N. Klenke and E. Giannini, "Development and Aging of ASR Mockups - Final Report EPRI Agreement No. 10003982," 2015.

[10] K. Freeseman, K. Hoegh and L. Khazanovich, "Characterizationof Concrete at Various Freeze-Thaw Damage Conditions Using SH-Waves," *Proceedings of the 42nd Review of Progress in Quantitative Nondestructive Evaluation (QNDE),* vol. July, pp. 26-31, 2015.

[11] K. Langenberg, R. Marklein and K. Mayer, "Ultrasonic Nondestructive Testing of Materials: Theoretical Foundations," CRC Press, 2012.

[12] F. Lingvall, T. Olofsson and T. Stepinski, "Synthetic Aperture Imaging Using Sources with Finite Aperture-Deconvolution of the Spatial Impluse Response," *J. Acoust Soc. America,* vol. 114, pp. 225-234, 2003.

[13] K. Hoegh, "Ultrasonic Linear Array Evaluation of Concrete Pavements - Thesis Dissertation," University of Minnesota, 2013.

[14] K. Hoegh and L. Khazanovich, "Extended Synthetic Aperture Focusing Technique for Ultrasonic Imaging of Conrete," *NDT & E International,* pp. 33-42, 2015.

[15] K. Freeseman, L. Khazanovich, A. Nojavan, A. Schultz and S. Chao, "Nondestructive Monitoring of Subsurface Damage Progression in Concrete Columns Damaged by Earthquake Loading," *Engineering Structures,* vol. 114, no. May, pp. 148-157, 2016.

[16] K. Freeseman, K. Hoegh, L. Khazanovich and H. Santos-Villalobos, "Nondestructive Analysis of Freeze Thaw Damage in Concrete Slabs Using Shear Waves," *Submitted to: ASCE Journal of Infrastructure Systems,* 2016.

[17] K. Hoegh and L. Khazanovich, "Correlation Analysis of 2S Tomographic Images for Flaw Detection in Pavements," J Test Eval, 2012.

[18] A. Peiffer, B. Kohler and S. Petzold, "The Acoustic Finite Integration for Waves of Cylindrical Symmetry (CAFIT)," *The Journal of the Acoustical Society of America,* vol. 102, pp. 697-706, 1997.

# Appendix A
# SAFT-Pan Reconstructions

# APPENDIX A. SAFT-PAN RECONTRUCTIONS

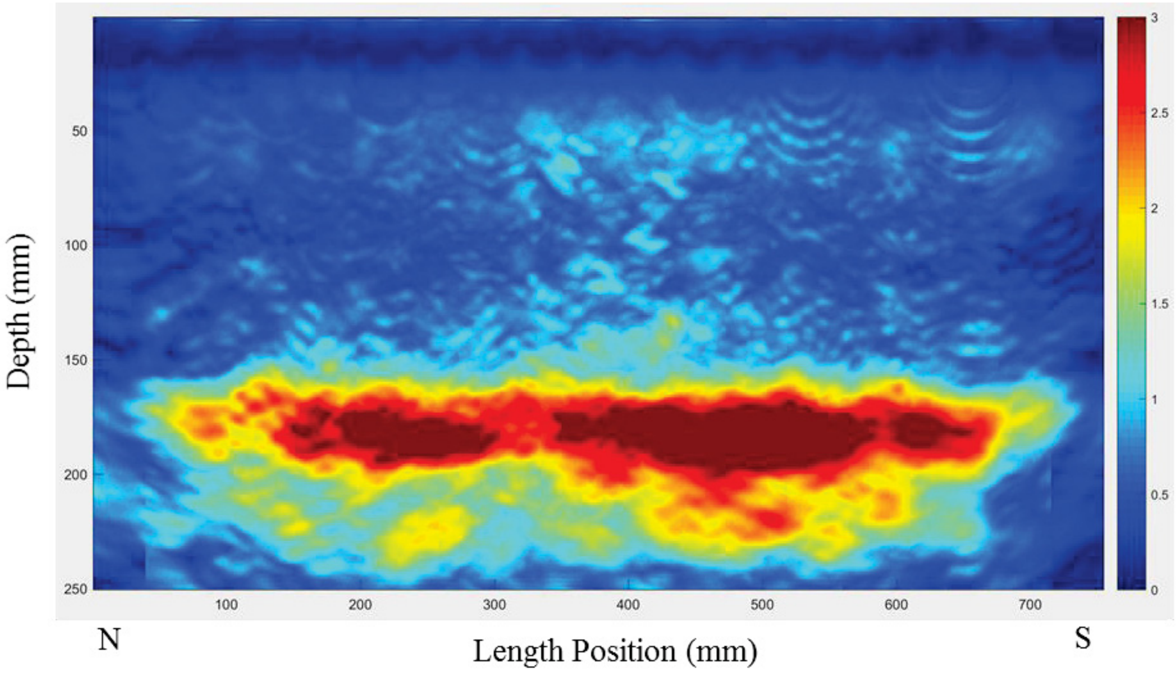

Fig. A. 1. SAFT-Pan Reconstruction of specimen Nefertiti, panoramic 1

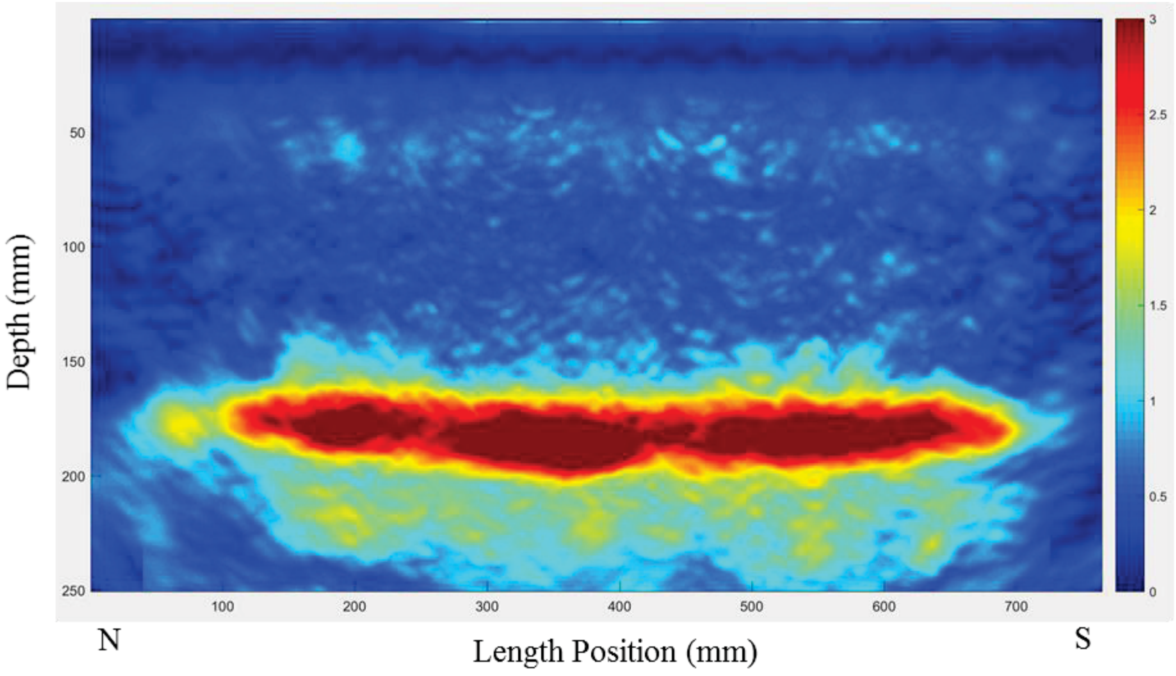

Fig. A. 2. SAFT-Pan Reconstruction of specimen Nefertiti, panoramic 2

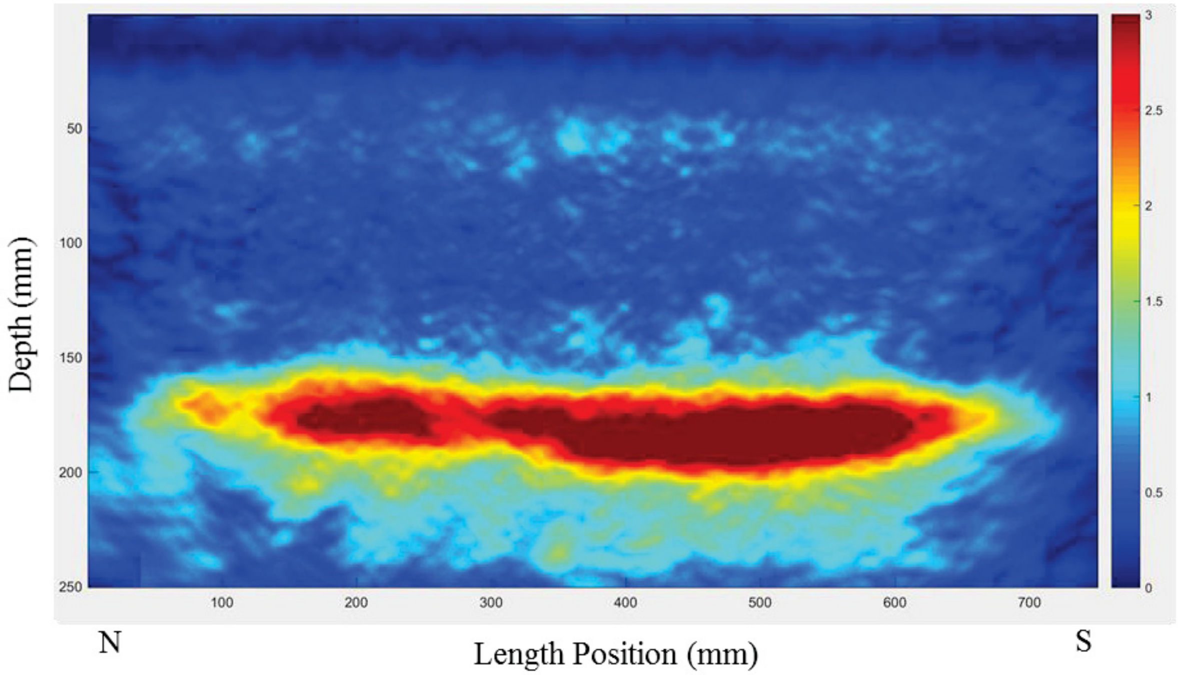

Fig. A. 3. SAFT-Pan Reconstruction of specimen Nefertiti, panoramic 3

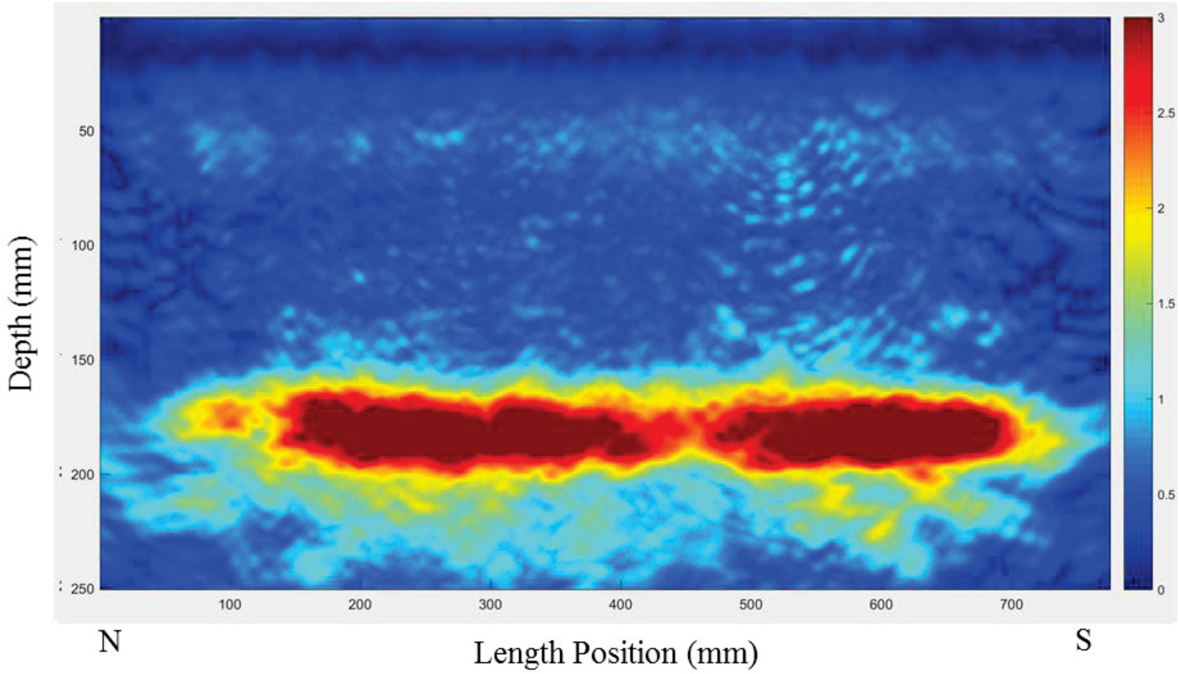

Fig. A. 4. SAFT-Pan Reconstruction of specimen Nefertiti, panoramic 4

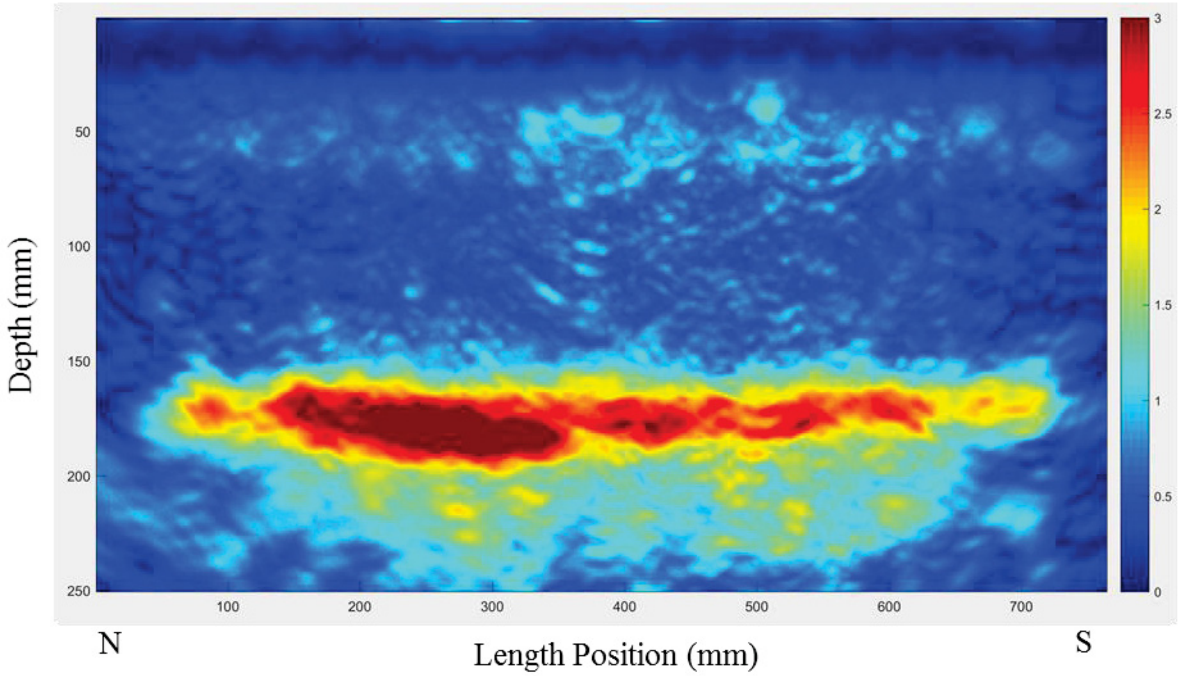

Fig. A. 5. SAFT-Pan Reconstruction of specimen Nefertiti, panoramic 5

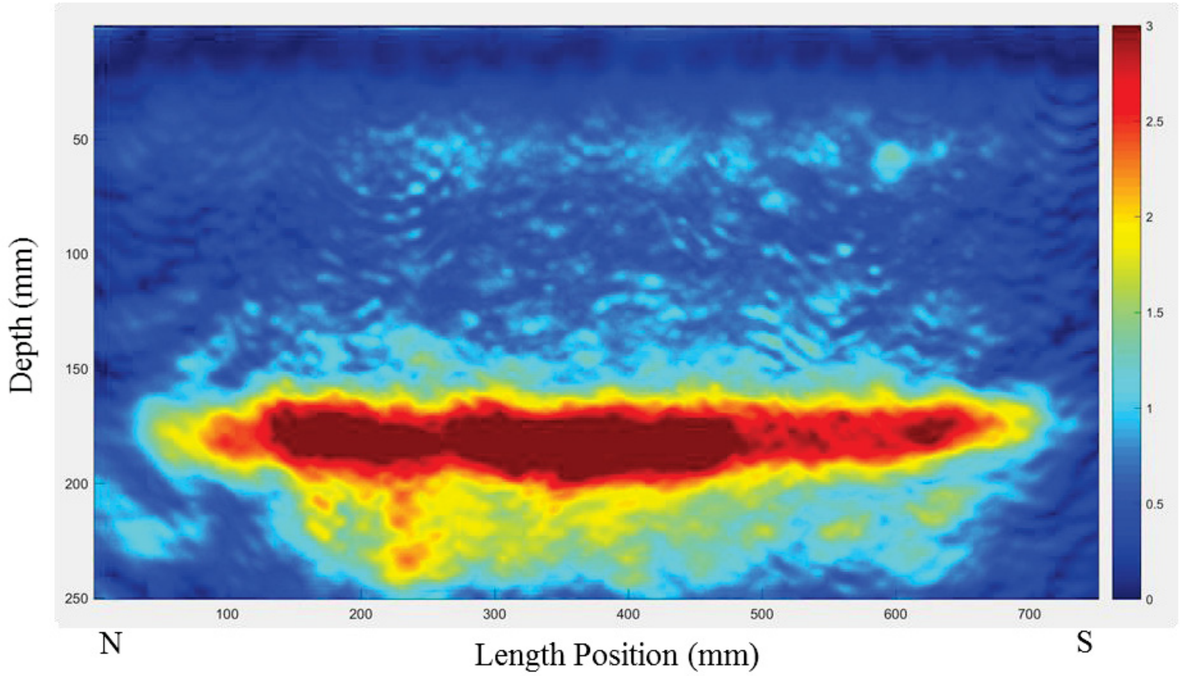

Fig. A. 6. SAFT-Pan Reconstruction of specimen Nefertiti, panoramic 6

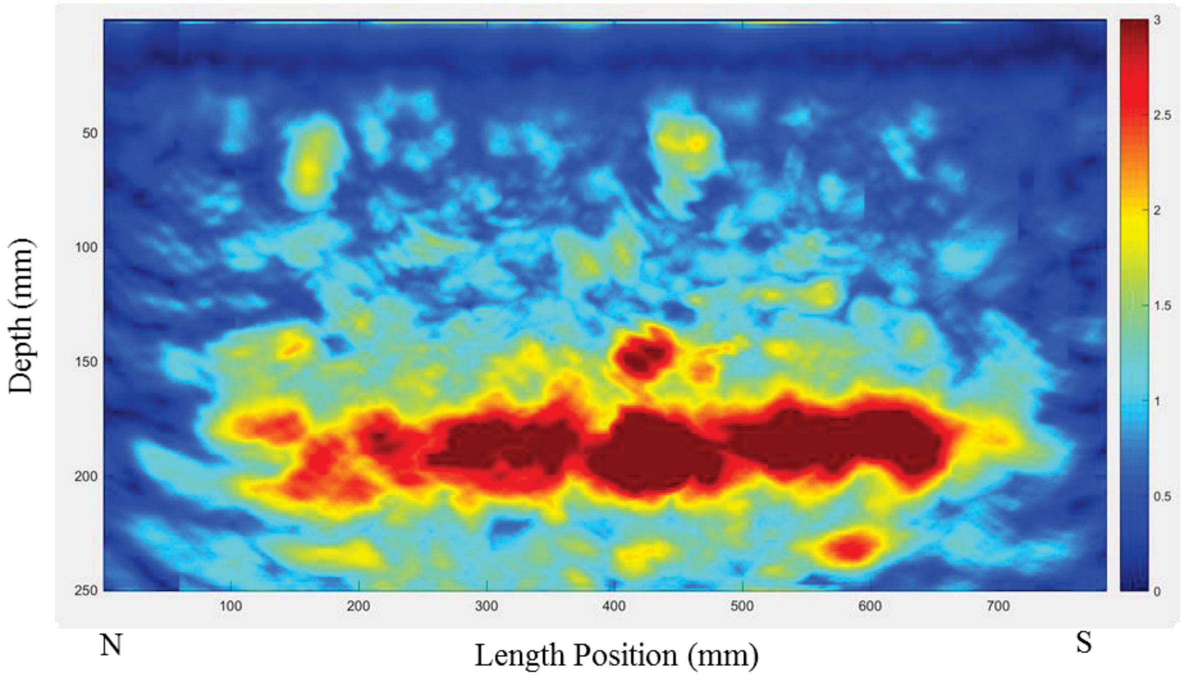

Fig. A. 7. SAFT-Pan Reconstruction of specimen Cleopatra, panoramic 1

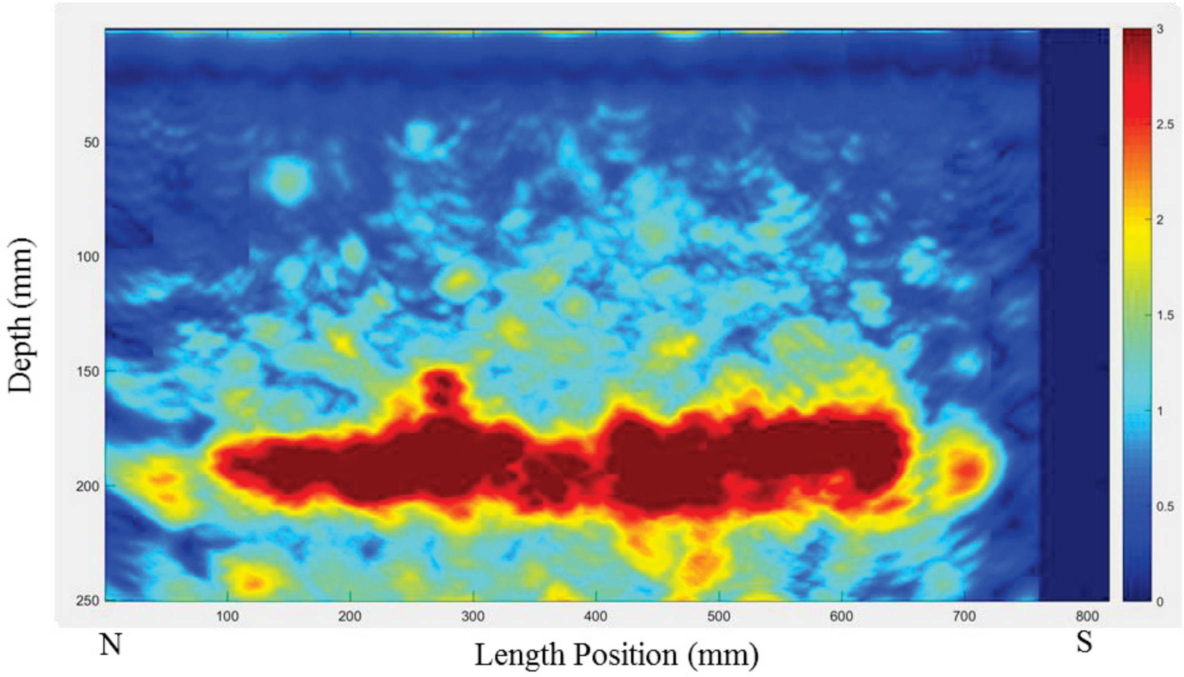

Fig. A. 8. SAFT-Pan Reconstruction of specimen Cleopatra, panoramic 2

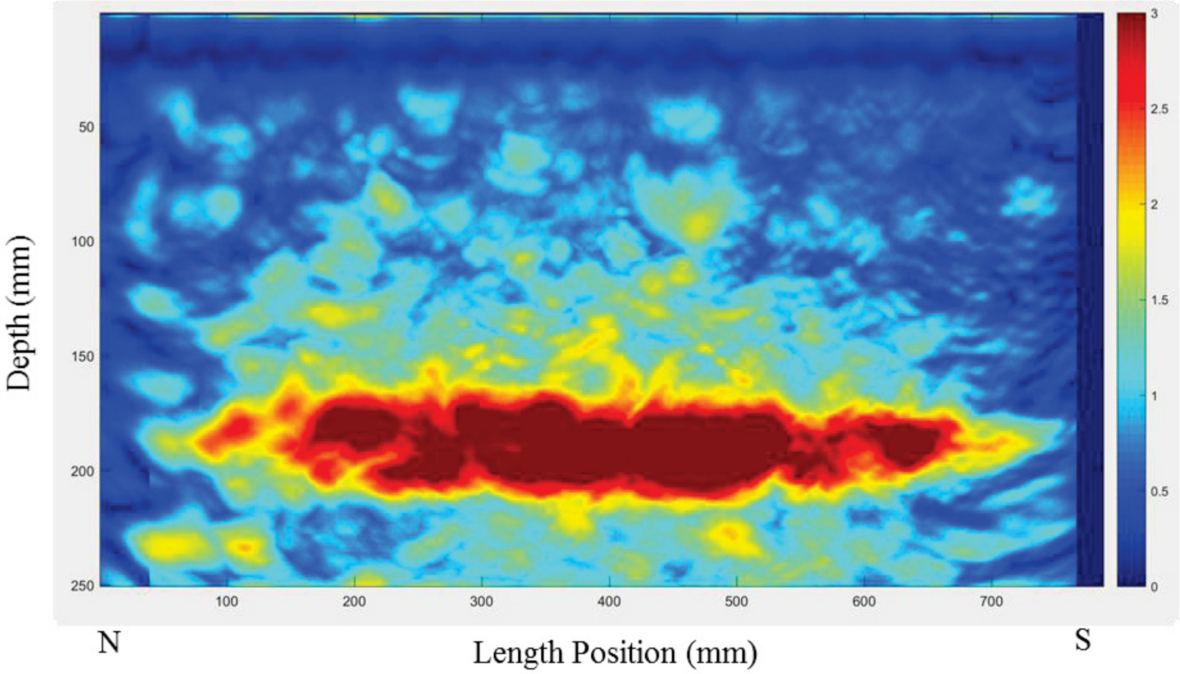

Fig. A. 9. SAFT-Pan Reconstruction of specimen Cleopatra, panoramic 3

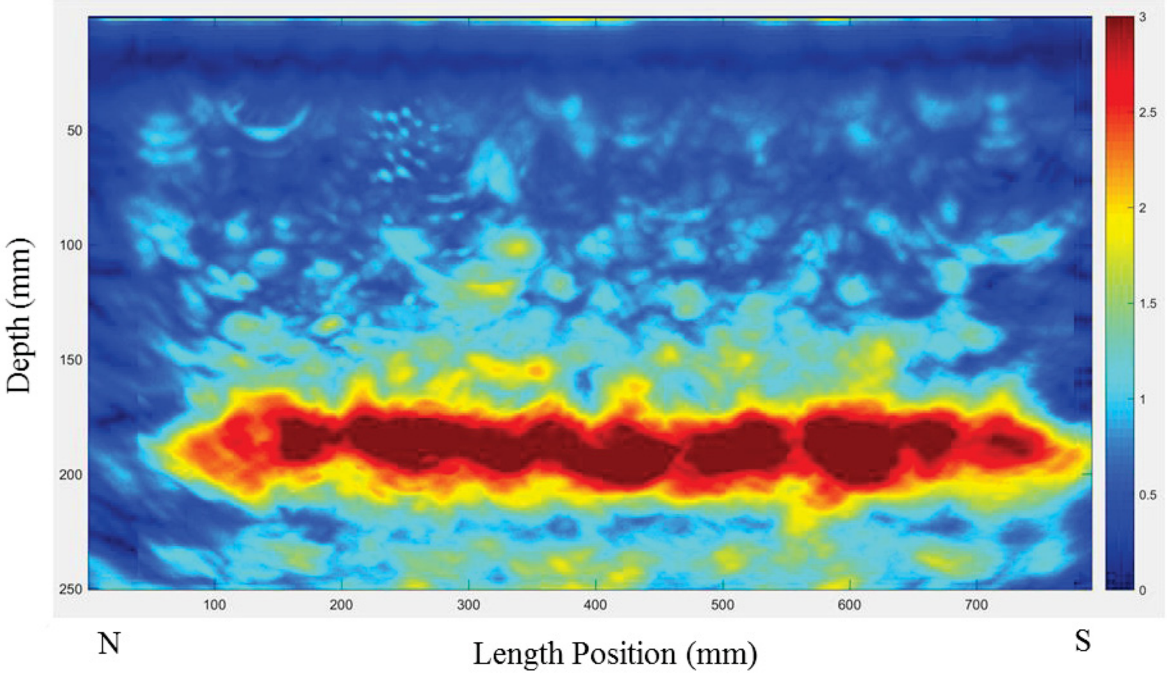

Fig. A. 10. SAFT-Pan Reconstruction of specimen Cleopatra, panoramic 4

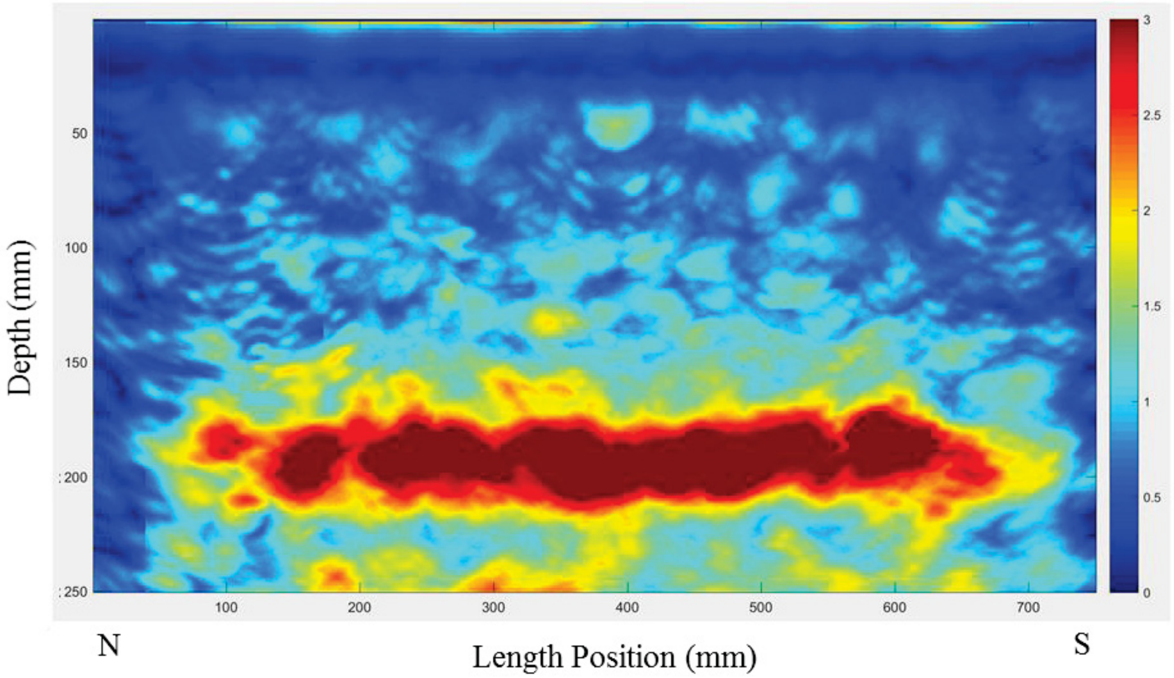

Fig. A. 11. SAFT-Pan Reconstruction of specimen Cleopatra, panoramic 5

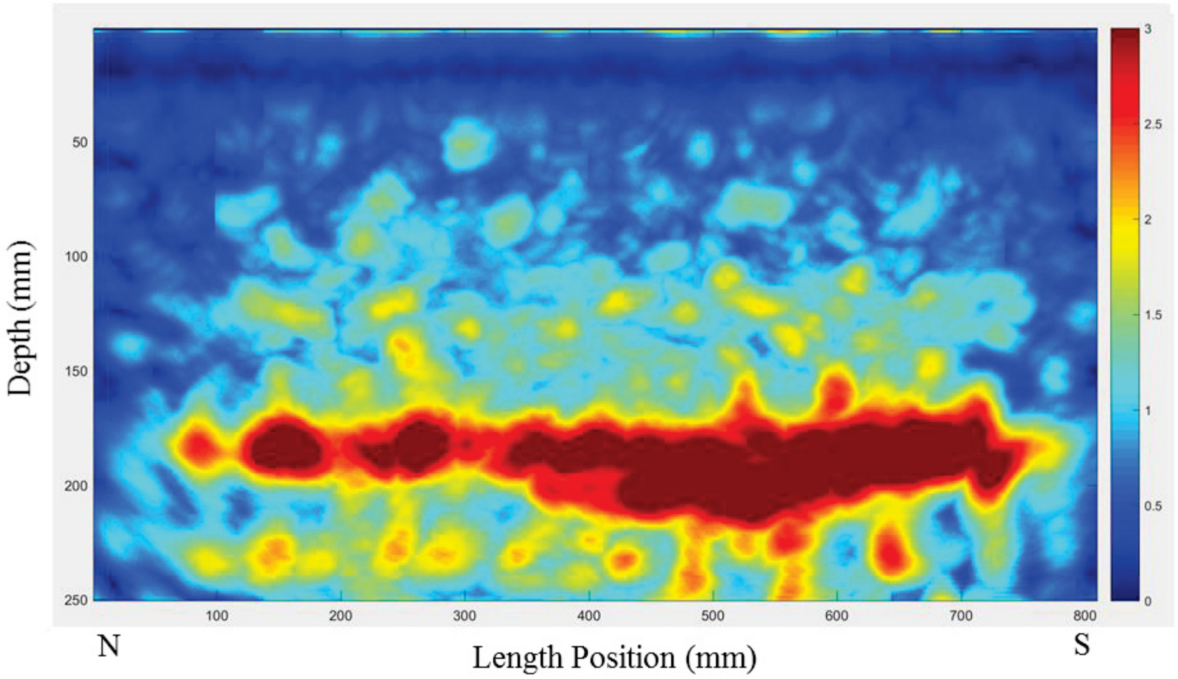

Fig. A. 12. SAFT-Pan Reconstruction of specimen Cleopatra, panoramic 6

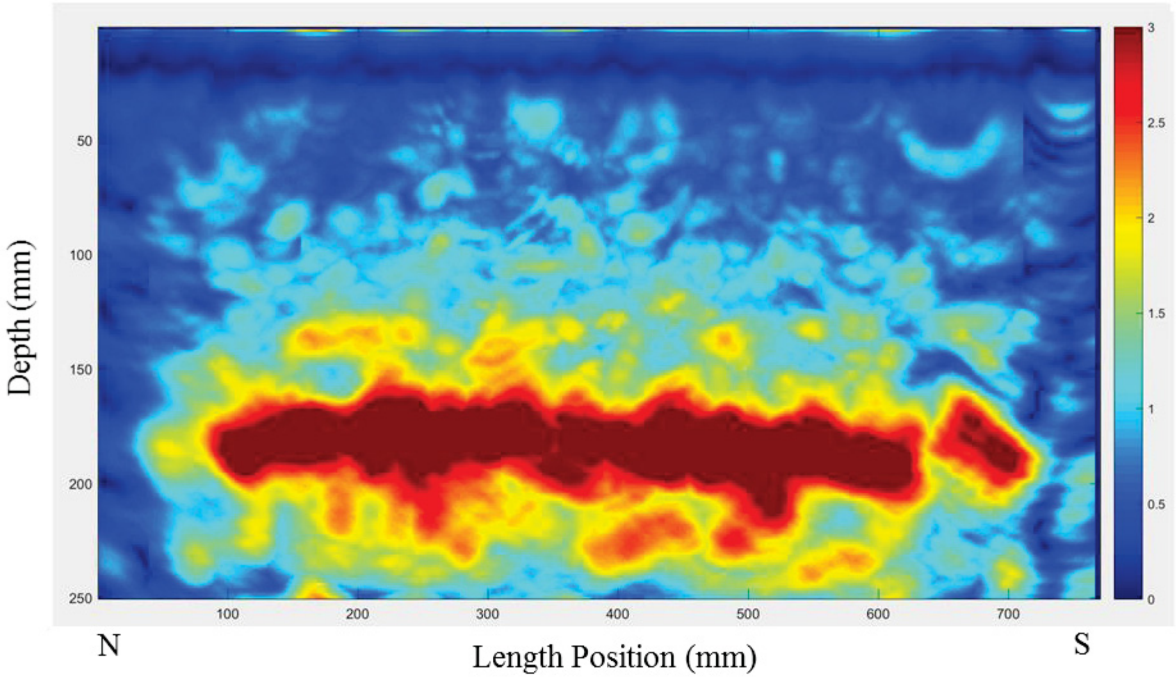

Fig. A. 13. SAFT-Pan Reconstruction of specimen Ramses, panoramic 1

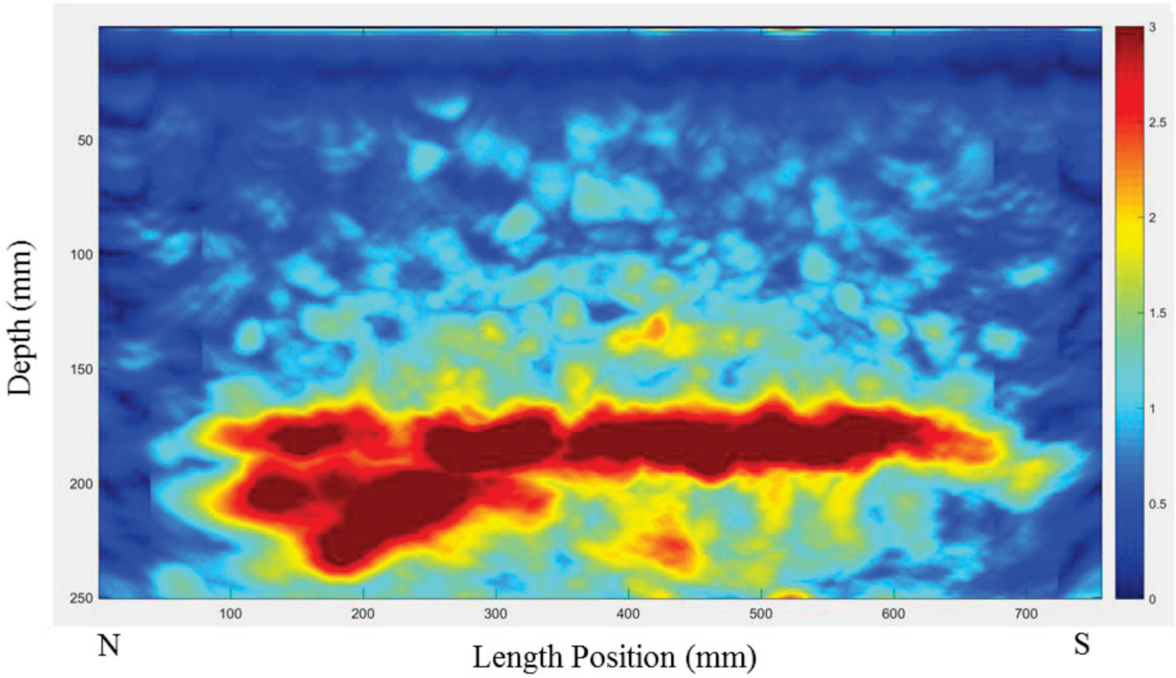

Fig. A. 14. SAFT-Pan Reconstruction of specimen Ramses, panoramic 2

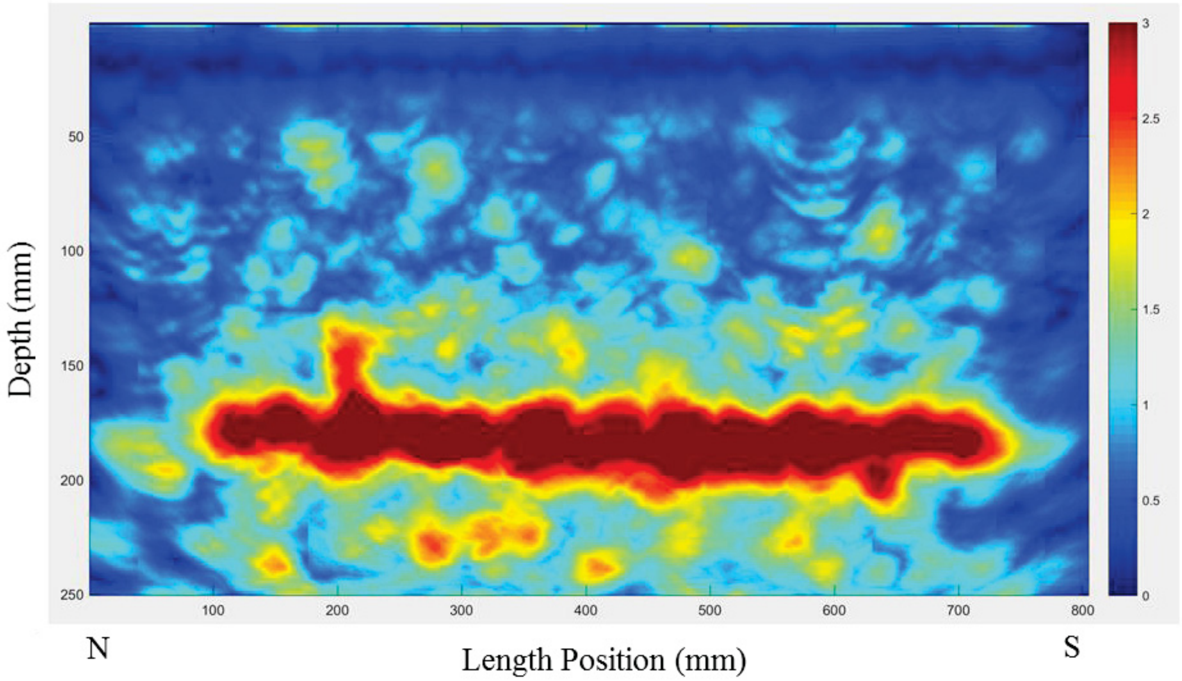

Fig. A. 15. SAFT-Pan Reconstruction of specimen Ramses, panoramic 3

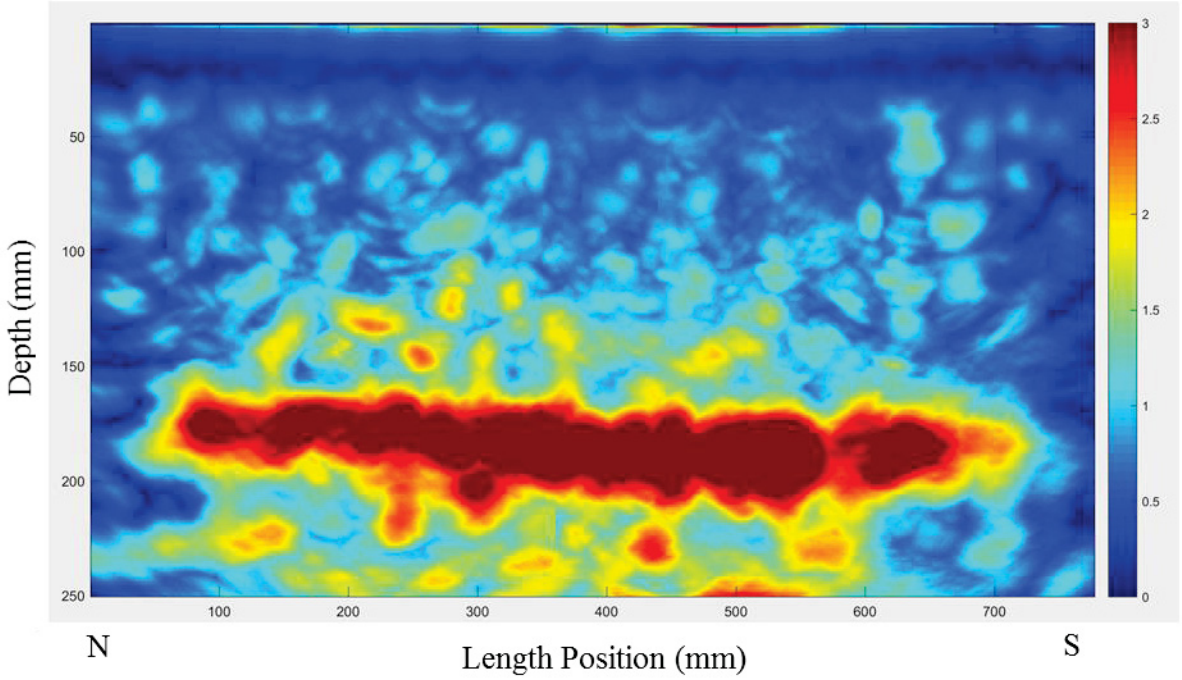

Fig. A. 16. SAFT-Pan Reconstruction of specimen Ramses, panoramic 4

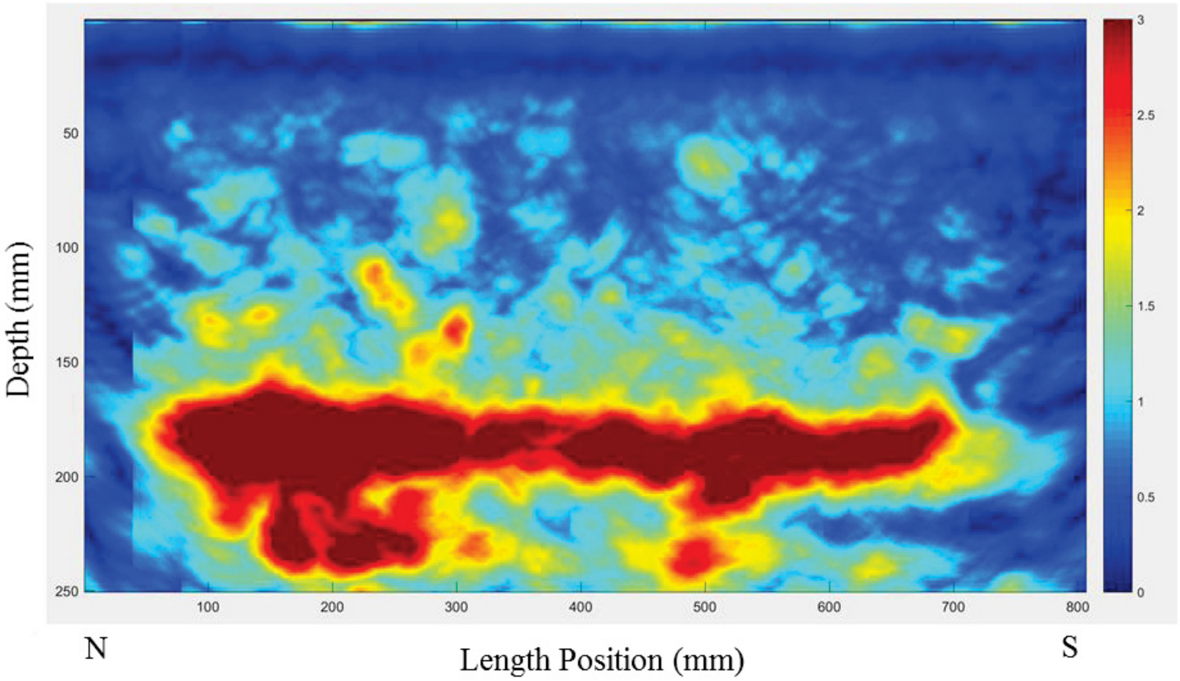

Fig. A. 17. SAFT-Pan Reconstruction of specimen Ramses, panoramic 5

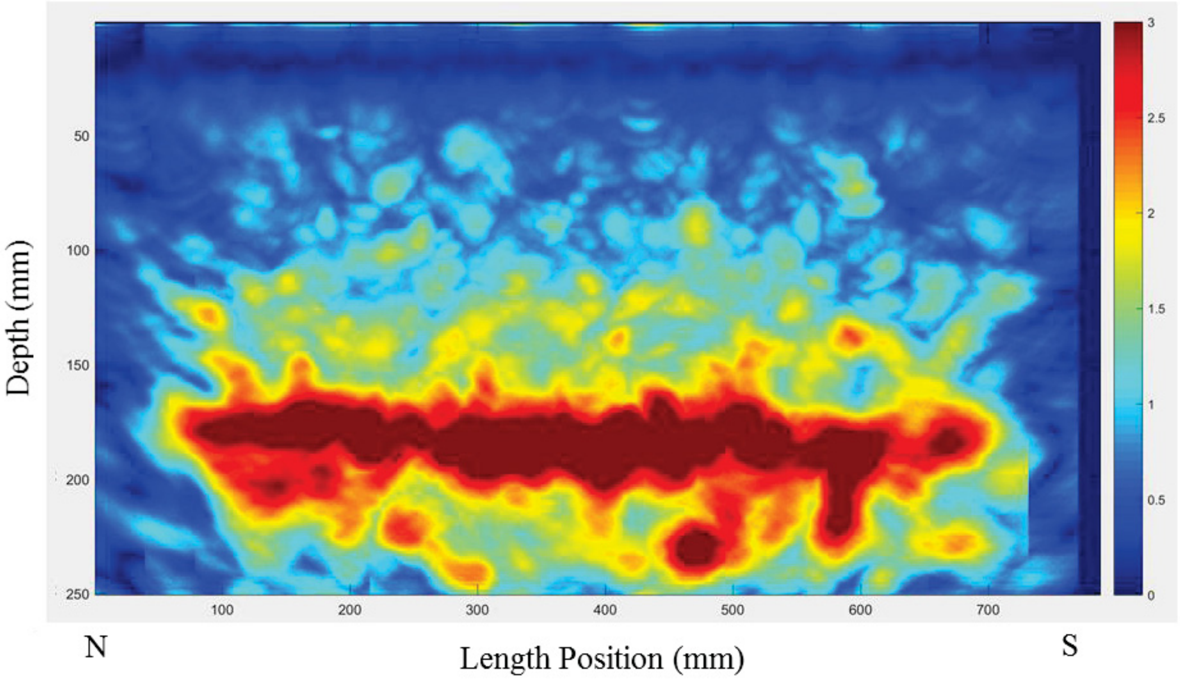

Fig. A. 18. SAFT-Pan Reconstruction of specimen Ramses, panoramic 6

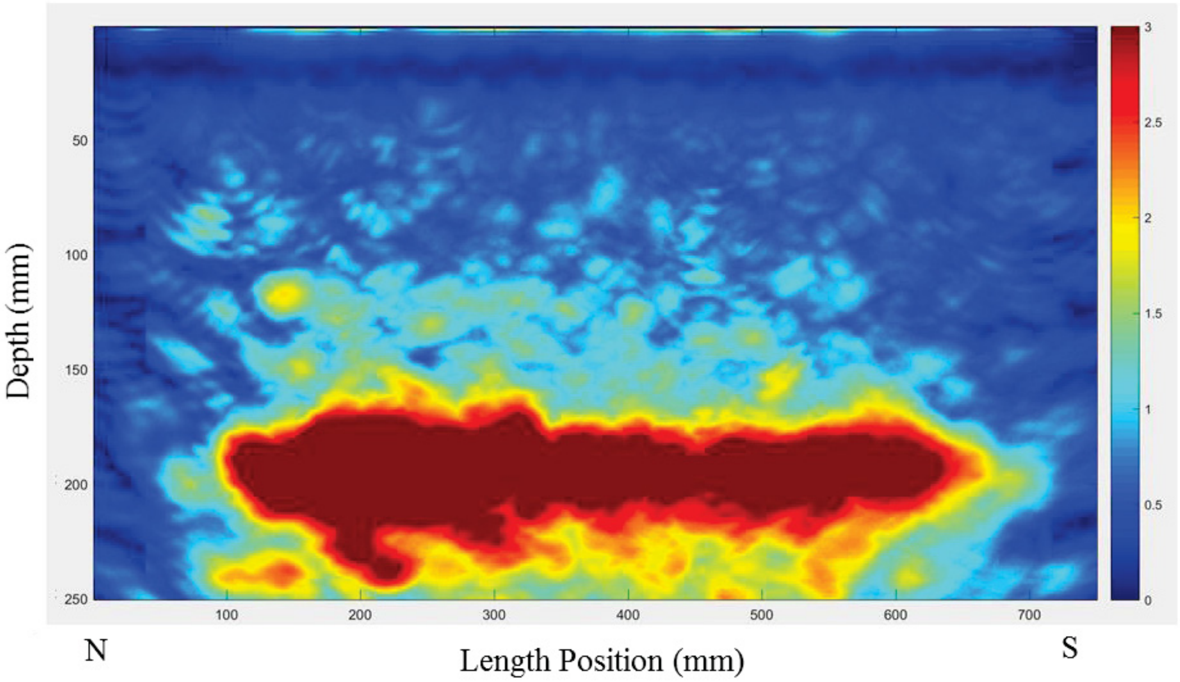

Fig. A. 19. SAFT-Pan Reconstruction of specimen King Tut, panoramic 1

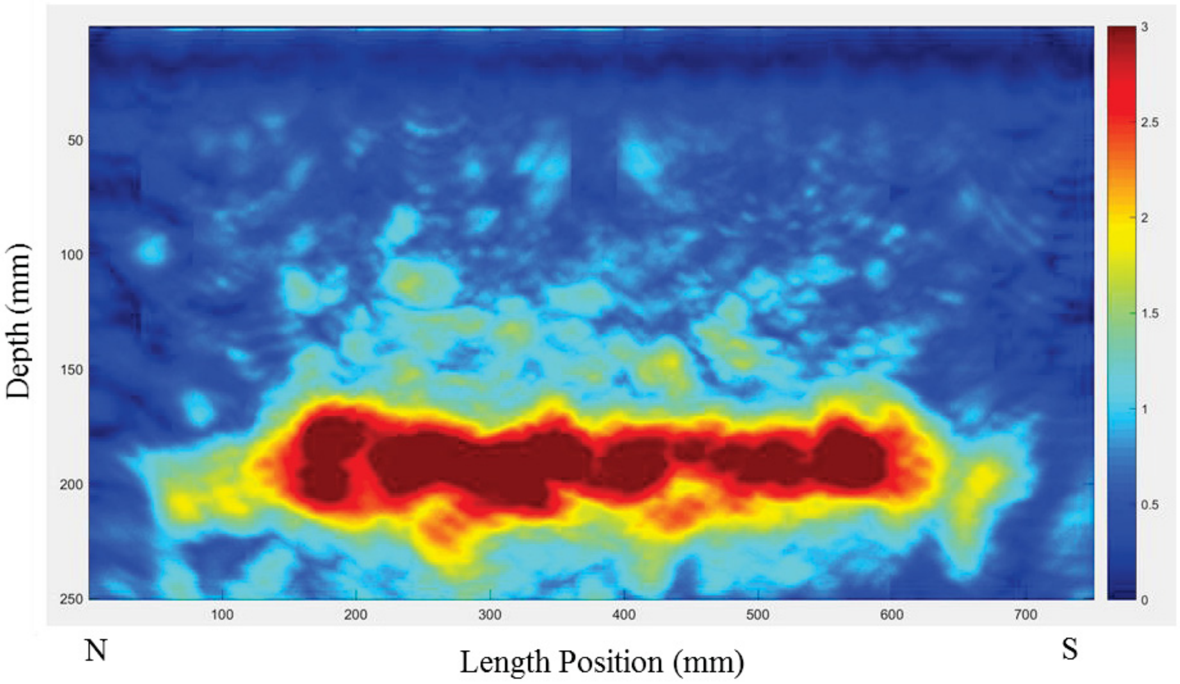

Fig. A. 20. SAFT-Pan Reconstruction of specimen King Tut, panoramic 2

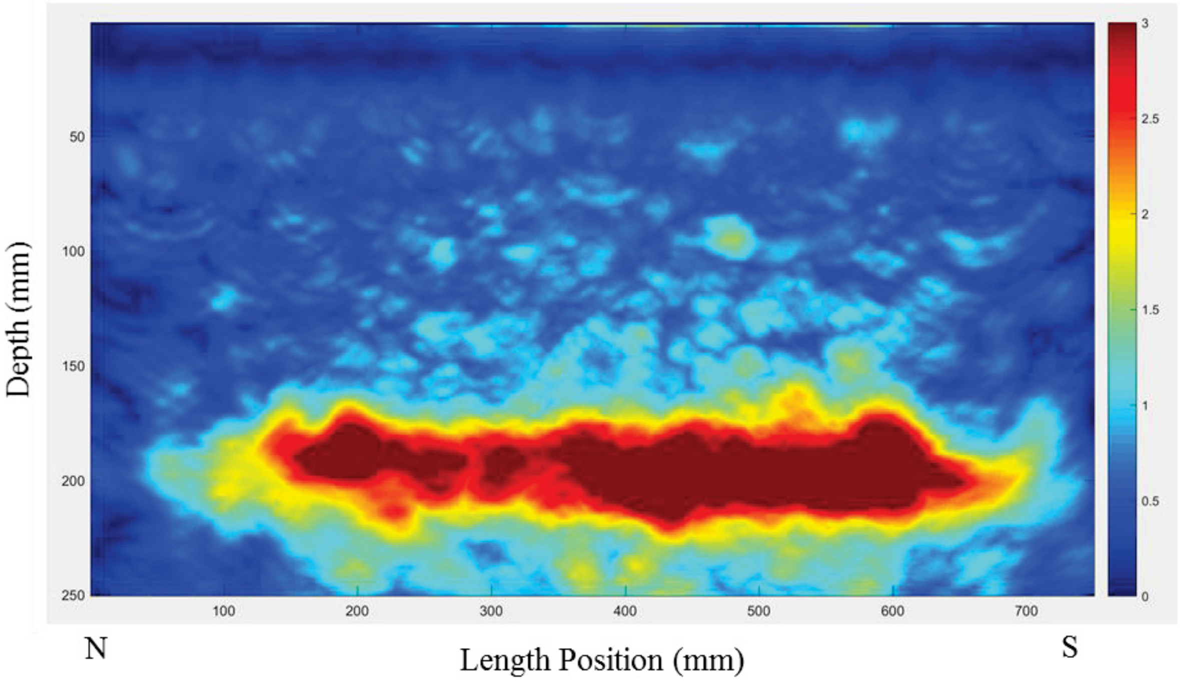

Fig. A. 21. SAFT-Pan Reconstruction of specimen King Tut, panoramic 3

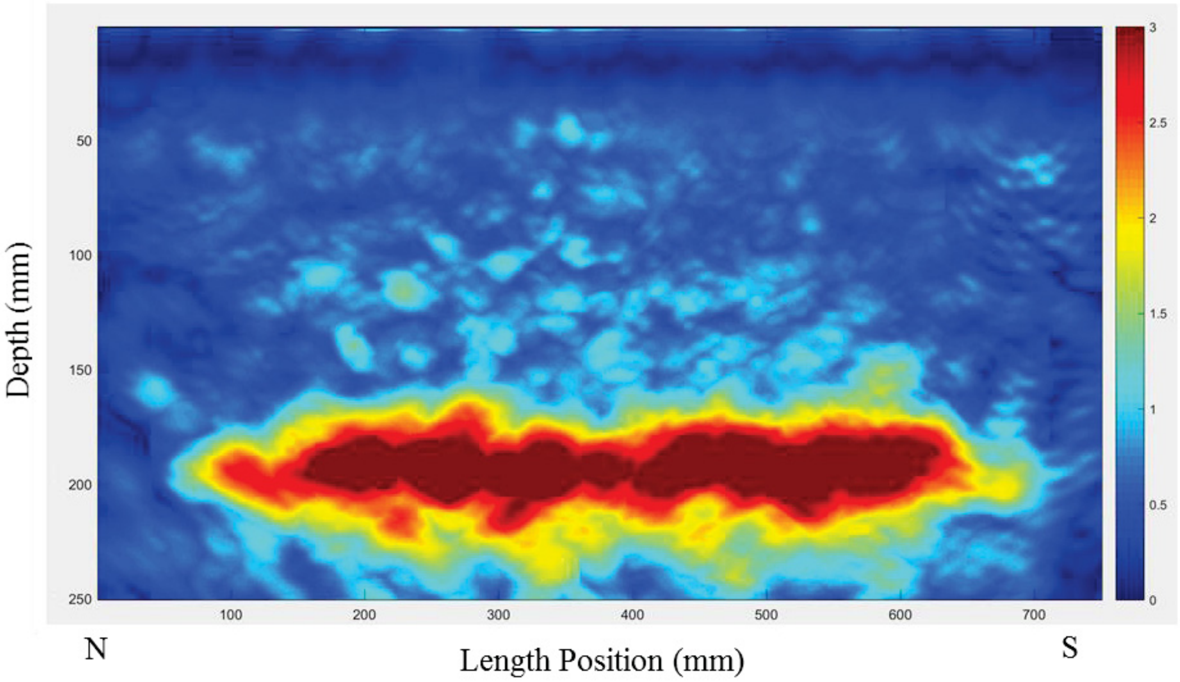

Fig. A. 22. SAFT-Pan Reconstruction of specimen King Tut, panoramic 4

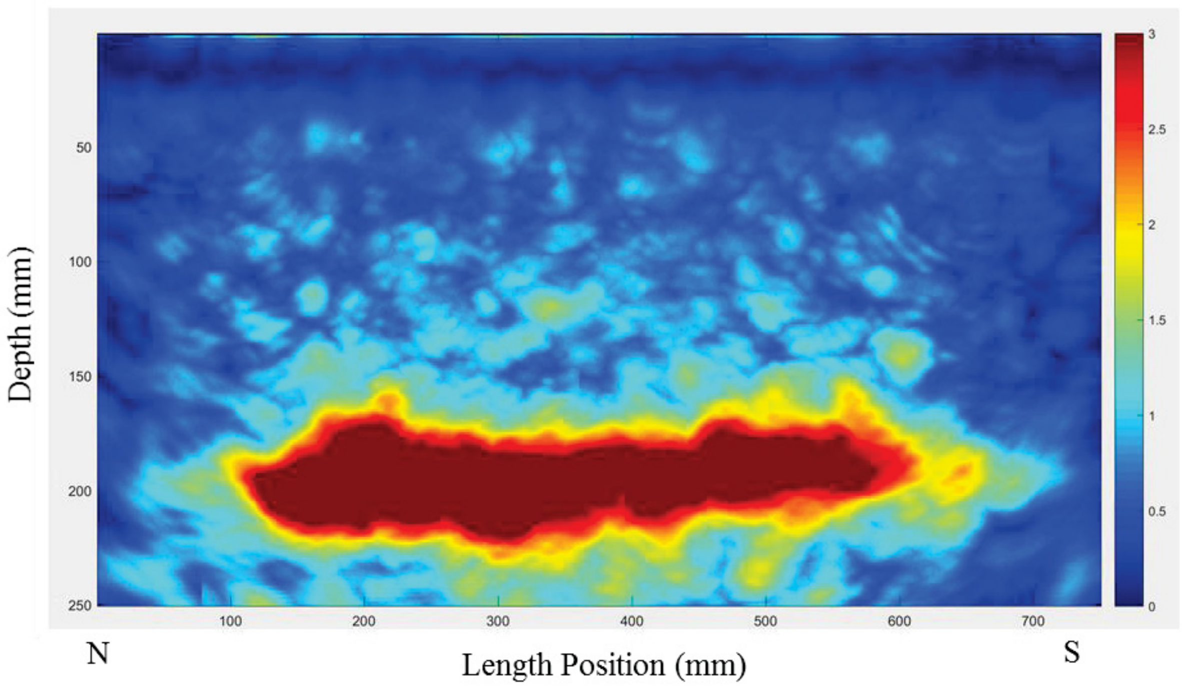

Fig. A. 23. SAFT-Pan Reconstruction of specimen King Tut, panoramic 5

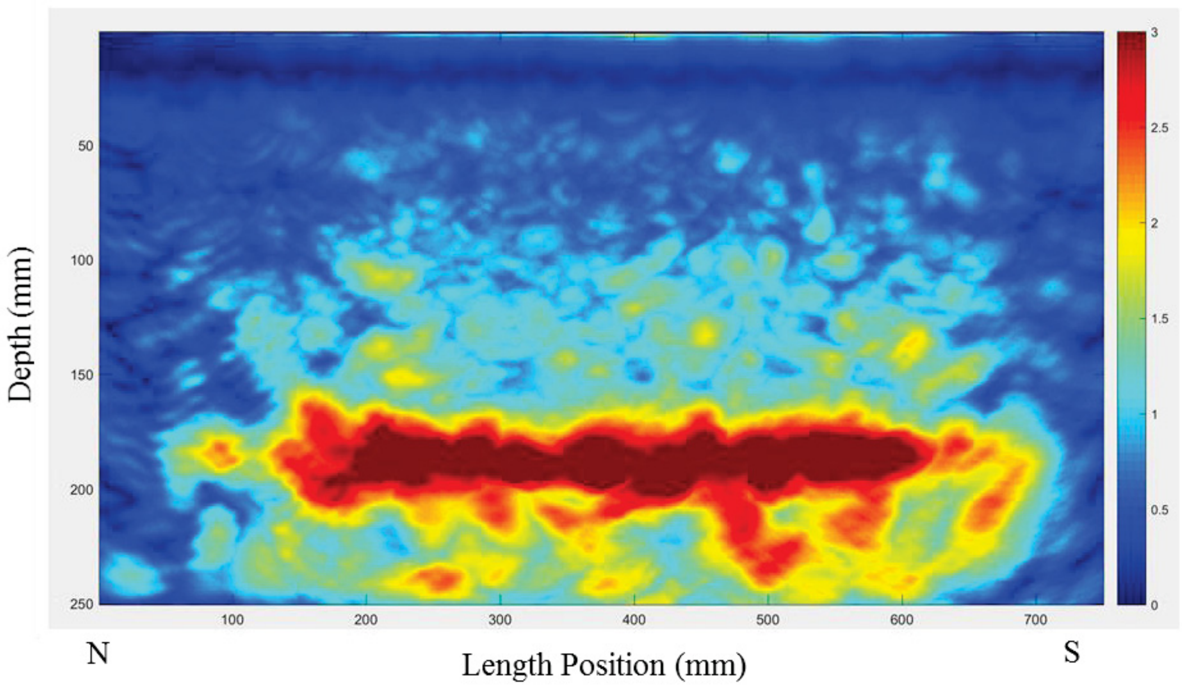

Fig. A. 24. SAFT-B Scan of specimen King Tut, panoramic 6